

A 4-6 GHz Radio Recombination Line Survey in the Milky Way*

HONG-YING CHEN,^{1,2,3,4} XI CHEN,^{5,2,6} JUN-ZHI WANG,^{5,6} ZHI-QIANG SHEN,^{5,6} AND KAI YANG^{5,3}

¹*Shanghai Astronomical Observatory, 80 Nandan Road, Xuhui District, Shanghai, 200030, China*

²*Center for Astrophysics, Guangzhou University, Guangzhou 510006, China*

³*University of Chinese Academy of Sciences, 19A Yuquanlu, Beijing 100049, China*

⁴*Jodrell Bank Centre for Astrophysics (JBCA), Department of Physics & Astronomy, Alan Turing Building, The University of Manchester, M13 9PL, United Kingdom*

⁵*Shanghai Astronomical Observatory, 80 Nandan Road, Xuhui District, Shanghai, 200030, China*

⁶*Key Laboratory of Radio Astronomy, Chinese Academy of Sciences, China*

(Received November 27 2019; Revised April 23, 2020; Accepted unknown)

ABSTRACT

We performed a radio recombination line (RRL) survey to construct a high-mass star-forming region (HMSFR) sample in the Milky Way based on the all-sky Wide-Field Infrared Survey Explorer (*AllWISE*) point source catalog. The survey was observed with the Shanghai 65m Tianma radio telescope (TMRT) covering 10 hydrogen RRL transitions ranging from H98 α to H113 α (corresponding to the rest frequencies of 4.5–6.9 GHz) simultaneously. Out of 3348 selected targets, we identified an HMSFR sample consisting of 517 sources traced by RRLs, a large fraction of this sample (486) locate near the Galactic plane ($|b| < 2^\circ$). In addition to the hydrogen RRLs, we also detected helium and carbon RRLs towards 49 and 23 sources respectively. We cross-match the RRL detections with the 6.7 methanol maser sources built up in previous works for the same target sample, as a result, 103 HMSFR sources were found to harbor both emissions. In this paper, we present the HMSFR catalog accompanied by the measured RRL line properties and a correlation with our methanol maser sample, which is believed to tracer massive stars at earlier stages. The construction of an HMSFR sample consisting of sources in various evolutionary stages indicated by different tracers is fundamental for future studies of high-mass star formation in such regions.

Keywords: recombination lines — stars: formation — ISM: molecules — radio lines: ISM

1. INTRODUCTION

Formation of high-mass stars in the giant molecular clouds, though intensively studied, remains mysterious (see review papers, e.g., Zinnecker & Yorke 2007; Tan et al. 2014). To reveal the intrinsic of high-mass star formation (HMSF) at the very early stage, the fundamental and vital step is to construct a complete sample of high-mass star-forming regions (HMSFRs). Ultra-compact HII regions (UCHIIRs) (< 0.1 pc) are hot ionized gas surrounding an exciting central high-mass star. Such regions are excited by an early O–B star from which the ultra-violet photons are strong enough to ionize neutral

hydrogen. HII regions spread widely at a Galactic scale and have strong luminosity across multiple wavebands (ultraviolet, visible, infra-red and radio), therefore, they are ideal tracers of HMSFRs.

HII region surveys in the Milky Way were firstly studied in visible wavelengths (Sharpless 1953, 1959; Gum 1955; Rodgers et al. 1960). However, the extinction in the optical largely limited the capability of such researches. The dust-free radio observations are therefore needed to construct a more complete sample of Galactic HII regions.

In 1965, radio recombination line (RRL) was firstly detected by Høglund & Mezger (1965) from M 17 and Orion A. Its thin optical depth in centimeter wavelengths makes it an optimal tracer of HII regions. RRL surveys were then performed in the next few decades, e.g. Mezger & Høglund (1967); Wilson et al. (1970);

Corresponding author: X. Chen
chenxi@gzhu.edu.cn

* a machine readable catalog accompanies this paper

Reifenstein et al. (1970); Downes et al. (1980); Caswell & Haynes (1987) and Lockman (1989). The properties of the Galactic RRLs, such as their spatial distribution, line widths, LSR velocities and intensities are probes of the morphological, chemical and dynamical information of the Milky Way (see Anderson et al. 2011). Thus, RRL is important in a range of astrophysical topics, such as the Galactic structure (e.g. Hou & Han 2015; Downes et al. 1980; Anderson & Bania 2009) and metallicity gradient across the Galactic disk which helps understanding the Galactic chemical evolution (GCE) (Wink et al. 1983; Shaver et al. 1983; Quireza et al. 2006; Balser et al. 2011).

More recent RRL surveys were performed with high-sensitivity facilities (e.g. Liu et al. 2013; Alves et al. 2015; Anderson et al. 2011, 2014). In particular, the recent Green Bank Telescope (GBT) HII Region Discovery Survey (HRDS) detected 603 discrete RRL components from 448 targets which were considered to be HII regions, thus doubled the number of known Galactic HII regions (Anderson et al. 2011). With the demonstration that HII regions can be reliably identified by their mid-infrared (MIR) morphology, Anderson et al. (2014) extended the HRDS sample to ~ 8000 candidate sources based on the *all-sky Wide-Field Infrared Survey Explorer* (*WISE*) MIR images (hereafter the Anderson2014 catalog). The Anderson2014 catalog contains ~ 1500 confirmed HII regions with observed RRL data in the literature, it is the most complete sample of HII regions to date.

The *WISE* data have four MIR bands: $3.4 \mu\text{m}$, $4.6 \mu\text{m}$, $12 \mu\text{m}$ and $22 \mu\text{m}$, with angular resolutions of $6''.1$, $6''.4$, $6''.5$ and $12''$, respectively, which are sensitive to HMSFRs. Its complete sky coverage and up-to-date database provide an optimal target sample for identifying HMSFR candidates. To further extended the HMSFR sample traced by RRLs beyond the Anderson2014 catalog, we conducted an RRL survey with the Shanghai 65m Tianma Radio Telescope (TMRT) based on the *WISE* point source catalog rather than the *WISE* MIR images. Since as HII regions form and evolve they will expand, selecting targets from the point source catalog will make our sample to include more compact, and therefore younger sources.

Comparing to other single-dish RRL surveys, we concentrate more on the correlation and association with methanol masers to signpost different periods of star-forming processes. Class II methanol maser is a powerful tracer of the hot molecular cloud phase of HMSFR (Minier et al. 2003; Ellingsen 2006; Xu et al. 2008), when there is significant mass accretion. HII region generally appears in more evolved phases of star formation, well

before the main sequence (Walsh et al. 1998; Bernasconi & Maeder 1996). As suggested by Churchwell (2002), due to beam-blending and thick optical depth, the densest and earliest HII regions are heavily obscured, more extended detectable UCHII regions probably are only formed until the central star reaches main sequence, and no longer accreting significant mass. By cross-matching the RRL and class II methanol maser samples, the evolutionary stages of their hosts may be specified more accurately. Therefore, simultaneous observation for both the RRLs and 6.7 GHz methanol masers were conducted to investigate their associations. Notably, due to beam dilution, RRL emissions from dense UCHII regions at earlier stages will be undetectable, thus our detected RRL sources will trace more extended and evolved HII regions. Previous studies have demonstrated that 6.7 GHz methanol masers can be excited in the UCHII regions, including both extended and compact sources identified by radio continuum data (e.g. Hu et al. 2016). Since RRL-detected UCHII regions are generally more evolved than those without RRL emissions, RRL researches will be helpful for identifying which methanol maser sources are at more evolutionary stages.

In this paper, we report the RRL detections with the measured line parameters, as well as the results of a correlation with the 6.7 GHz methanol maser sample towards the same target sample built by Yang et al. (2017, 2019). Section 2 describes the sample selection and observations. Section 3 presents the results of the survey followed by a discussion in section 4. We summarize our main conclusions in Section 5.

2. OBSERVATIONS AND DATA REDUCTION

2.1. Source Selection

RRLs and 6.7 GHz methanol masers were observed simultaneously in our survey. The targets were selected with the following methodology: firstly, a cross-matching was applied between the 6.7 GHz methanol maser catalog created by the Methanol Multi beam (MMB) Survey conducted with the Parkes telescope (Caswell et al. 2010, 2011; Green et al. 2010, 2012; Breen et al. 2015), and the *All-WISE* point source catalog. As a result, there are 502 MMB maser sources which have a *WISE* counterpart with a spatial offset within $7''$. We only kept 473 sources with *WISE* data available from all four bands. A magnitude and color-color analysis was then applied to those 473 sources (see Yang et al. 2017 for details). 73% of those sources fell in the color region with well-constrained *WISE* color criteria: $[3.4] < 14 \text{ mag}$; $[4.6] < 12 \text{ mag}$; $[12] < 11 \text{ mag}$; $[22] < 5.5 \text{ mag}$; $[3.4] - [4.6] > 2$, and $[12] - [22] > 2$. To avoid repetition,

we excluded sources locating in the MMB survey region ($20^\circ < l < 186^\circ$ and $|b| > 2^\circ$). Due to the limitation of observing range, we also excluded those with a declination below -30° . In total, 3348 *WISE* point sources were selected searching for RRLs and methanol maser emissions. In this sample, 1473 sources are located at a high Galactic latitude region with $|b| > 2^\circ$ and 1875 sources fall within $\pm 2^\circ$ of the Galactic Plane.

Among the selected targets, Yang et al. (2017, 2019) detected 6.7 GHz methanol masers from 241 sources, 209 of them are near the Galactic Plane where $|b| < 1^\circ$.

2.2. Observation & Data Reduction

The observations were performed between 2015 September and 2018 January with the 65m TMRT in Shanghai, China (Yang et al. 2017, 2019). A cryogenically cooled C-band receiver (4-8 GHz) with two orthogonal polarizations was employed in this survey. We used an FPGA-based spectrometer Digital Backend System (DIBAS) (VEGAS; Bussa & VEGAS Development Team 2012) to receive and record the signals. A total of 16 spectral windows were applied in the observations, each has 16384 channels and a bandwidth of 23.4 MHz supplying a velocity resolution of $\sim 0.1 \text{ km s}^{-1}$ at 4.5 GHz. Ten of the spectral windows were set up to cover hydrogen RRL transitions spanning from H98 α to H113 α as specified in Table 1. In addition to RRLs, the 6.7 GHz methanol maser (CH₃OH) emission line, 4.8 GHz H₂CO emission and absorption lines, as well as the 4.7 and 6.0 GHz excited-state OH maser transitions were also observed. The observed 6.7 GHz methanol maser results are reported in Yang et al. (2017, 2019). This paper mainly focuses on RRL detection and a cross-match between RRLs and methanol masers. In the observations, the system temperature is about 20 \sim 30 K and the main beam efficiency of the TMRT is $\sim 60\%$. The beam has a full width at half-maximum (FWHM) of $\sim 3' - 4'$ at the frequencies of RRLs. There is an uncertainty of $< 20\%$ in the detected flux densities for the sources estimated from the observed variation of the calibrators.

A position-switching mode was applied in the observations. Each source was observed with two ON-OFF cycles, both the ON- and OFF-positions in each cycle take ~ 2 minutes. To ensure data reliability, sources with bad data quality (eg. radio frequency interferences (RFI), high noise level or abnormal signals) were re-observed with many more cycles. For each source, we primarily set the OFF-point to $(0.0^\circ, -0.4^\circ)$ away from the ON-position in (R.A., Decl.). Sources with OFF-positions showing RRL emission were re-observed with a

different OFF-position to exclude the background emissions. In total, the observations took ~ 700 hours of observing time excluding calibrations.

The data were processed with the GILDAS/CLASS¹ software package (Pety 2005; Gildas Team 2013). Adjacent Hn α transitions with large quantum numbers ($n > 50$) have similar line properties, such as line intensity and FWHM line width (see Balser 2006). Therefore, the spectra of the observed 10 transitions through H98 α to H113 α can be averaged to achieve a higher S/N. After averaging over the 10 RRL transitions at two polarizations, a typical $3\text{-}\sigma$ sensitivity of $\sim 7 \text{ mK}$ per channel was achieved for the majority of our sources.

Due to different rest frequencies, the 10 RRL transitions have different velocity resolutions in their individual spectrum. When averaging over the spectral windows, the GILDAS/CLASS software will resample the data with the coarsest resolution of them. Depending on the spectral quality, we typically smooth the averaged spectrum over 5 to 30 channels to have a spectral resolution of ~ 0.4 to $\sim 2.4 \text{ km s}^{-1}$. After that, depending on the background fluctuations, the spectral baselines were subtracted by a first or multi-order (< 4) polynomial fitting. Then the line profiles were fitted with a Gaussian model. For the multi-component sources, the number of Gaussian components was decided via a visual inspection. Notably, it is somehow hard to disentangle the blended line components which have very close central frequencies, so some of the blended sources may be identified as single emission with wide line width (see Section 3.1). The Gaussian fitting results are reported in Section 3.

3. RESULT

3.1. RRL Detections

A summary of RRL detections in this work and 6.7 GHz methanol maser detections from Yang et al. (2017, 2019) are presented in Table 2. Out of the 3348 targets, we detected hydrogen (H) RRL emissions from 527 positions, corresponding to a detection rate of 15.7%. Excluding the potential Planetary Nebula (PNe) and Supernova Remnant (SNR) (see Sec. 3.2), we built a sample of 517 HMSFRs based on the RRL detections. The derived line parameters and source information for the H RRLs from the HMSFR sample are listed in Table 3. The spectra for all the detected RRLs (including helium (He) and carbon (C) RRLs; see Section 4.3) are given in Appendix A. Amongst the 517 HMSFR candidates, 488

¹ <https://www.iram.fr/IRAMFR/GILDAS/>

Table 1. The information of the spectral windows of the TMRT receiver we applied in this survey.

Window Number	1	2	3	4	5	6	7	8
ν_o (MHz)	4497.78	4593.09	4618.79	4758.11	4829.66	4874.16	5008.92	5148.7
Line Name	H113 α	H $_2^3$ CO	H112 α	OH	H $_2$ CO	H110 α	H109 α	H108 α
Window Number	9	10	11	12	13	14	15	16
ν_o (MHz)	6016.75	6032.92	6049.08	6106.85	6289.14	6478.76	6672.30 (6676.08)*	6881.49
Line Name	OH	OH	OH	H102 α	H101 α	H100 α	CH $_3$ OH & H99 α	H98 α

*The 15th spectral window covers both the 6.7 GHz methanol maser and H99 α line, we set the central frequency of the window to the medium value of the two lines.

Table 2. Overview of the main detection results.

Total HMSFRs	HMSFRs traced by RRLs	Maser associations	Maser-only sources	He α lines	C α lines	SNR	PNe
(1)	(2)	(3)	(4)	(5)	(6)	(7)	(8)
654	517	103	137	49	23	5	5

NOTE—Overview of the main results: (1) the final HMSFR sample combing those traced by RRL and/or 6.7 GHz methanol maser reported in Yang et al. (2017, 2019), (2) HMSFRs traced by RRL detections excluding potential PNe and SNRs, (3) HMSFR sources associated with both RRL and 6.7 GHz methanol maser, (4) HMSFRs associated only with 6.7 GHz methanol maser, (5) helium recombination lines and (6) carbon recombination lines, (7) SNR and (8) PNe candidates catalogd in SIMBAD.

of them reside within $|b| < 2^\circ$, only 28 are from higher Galactic latitude regions ($|b| > 2^\circ$). Combining with the 240 methanol maser sample in Yang et al. (2017, 2019), excluding one associated with a potential SNR, there are 654 HMSFR sources traced by RRLs and/or methanol maser listed in Table 4.

We cross-matched our detected sources with the Anderson2014 catalog consisting of ~ 8000 sources. Due to the lack of radio observations, only ~ 1500 sources in their sample were confirmed to be “Known” HII regions (denoted as “K” sources in Table 2 of Anderson et al. 2014). For targets which spatially associate with multiple sources in the Anderson2014 catalog, “Known” sources would be designated preferentially. For targets associate with multiple “Known” sources or other types of Anderson2014 sources, the closest Anderson2014 counterpart would be designated. There are 467 HMSFR candidates in our sample which are associated with at least one of Anderson2014 sources within a separation of $3'$ (corresponding to the beam size of TMRT) plus the radius of the Anderson2014 source. Amongst them, 425 were classified as “known” HII regions, we thus confirmed the other 42 sources being HII regions. For the sources included in the Anderson2014 catalog, we label their type accordingly in Column (11) of Table 3. There are also 3 PNe and 4 SNR candidate sources associated with Anderson2014 sources, due to the extended morphology of HII regions, these targets may be

overlapped with the Anderson2014 sources along the line of sight (LOS).

There are 133 sources showing multiple (typically two or three) H RRL emission components. Figure 1a shows an example spectrum for such sources. The multiple RRL components may arise from nearby HII regions within the TMRT beam or overlapped HII regions along the LOS. Diffused ionized gas leaked from nearby HMSFRs may also cause multi-components in the RRL spectra (Zavagno et al. 2007; Anderson 2010; Oey & Kennicutt 1997). Some components have line emissions with close peak velocities causing confusion with a wide line width or non-Gaussian profile. An example of this is presented in Figure 1b.

Notably, RRL detections at adjacent observing positions with similar peak velocities are possibly from the same extended HII region. Moreover, HII regions with large angular size may have leaked RRL emission detected by the side lobe of the telescope when observing its nearby target points. Those RRL components have similar line velocities but much weaker line intensities comparing to the emission from the central position of the source. There are 5 RRL sources which were potentially detected by the side lobe, we label those emissions as possible duplicated sources by “SL” and the name of the real source in Column (11) in Table 3.

Our RRL detections have peak intensities ranging from 0.01 to 2 K with an average value of 0.07 K, and

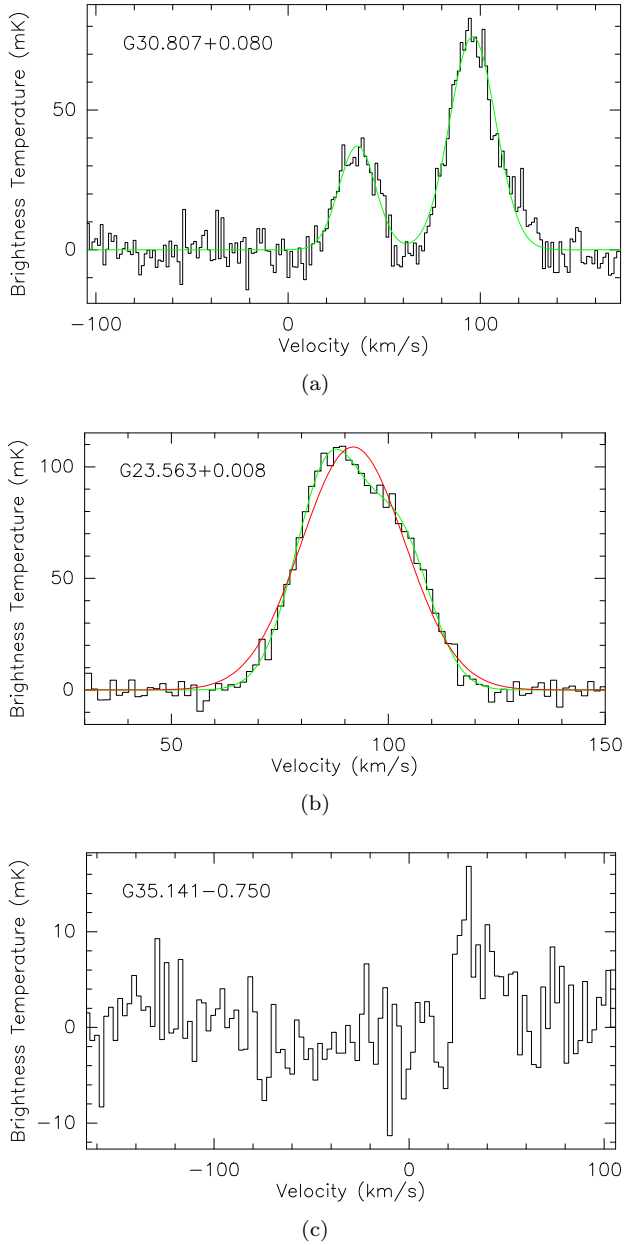


Figure 1. Example spectra of the detected hydrogen RRLs: (a) a source with two explicit Gaussian line components; (b) a non-Gaussian line component possibly caused by two very close RRL emissions with a velocity offset smaller than their width; and (c) a weak RRL signal. The spectra for the whole RRL sample can be found in the Appendix A.

an integrated intensity from 0.1 to 58 $\text{K}\cdot\text{km s}^{-1}$ with an average of $1.9 \text{ K}\cdot\text{km s}^{-1}$. Among the 517 HMSFR candidates, there are 12 weak sources, labeled with “?” in column (11) in Table 3, which have a line intensity only slightly above our 3σ detection threshold, no accurate Gaussian fitting results can be achieved for them. For those weak sources, we only give their peak intensity in

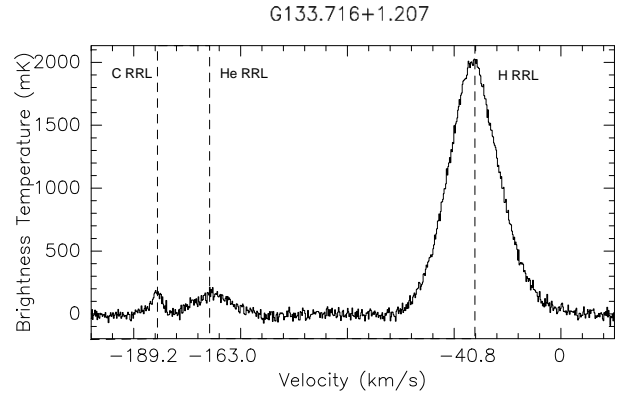


Figure 2. An example source with the three atomic RRL detections. Helium and carbon RRLs generally have a constant velocity offset with respect to hydrogen RRLs of -122 km s^{-1} and -149 km s^{-1} respectively. The spectra for the whole RRL sample can be found in the Appendix A.

Table 3. Further observations with longer integration time are required for them to get a higher S/N. Figure 1c illustrates an example of these weak sources. In addition to the 12 weak sources, for multi-component sources containing such weak line component(s), we only provide Gaussian fitting results for the stronger components.

In addition to H RRL transitions, the 23.4 MHz spectral windows (see Section 2.2) also simultaneously cover the rest frequencies of the nearby He and C RRLs, they have the same intrinsic quantum numbers with the H RRLs within each spectral window. In the velocity domain, He and C RRLs typically have a constant velocity offset with respect to H RRLs of -122 km s^{-1} and -149 km s^{-1} , respectively. The derived line parameters of He and C RRLs are given in Table 5. Figure 2 shows an example source with all the three atomic RRLs. In total, we found 49 He RRLs and 23 C RRLs in the observed sample (see Section 4.3 for further discussions).

3.2. Other Sources

In addition to HMSFRs, ionized gas associated with other astrophysical objects such as planetary Nebula (PNe) and Supernova Remnant (SNR) can also produce RRLs. We performed a matching analysis for our sample with the SIMBAD² catalog to exclude previously known PNe and SNR sources with a positional criterion of $< 3'$. We mark sources with an explicit PNe or SNR identifier as “PNe” or “SNR” in Tables 6 and 7, respectively. To maximize the reliability of our HMSFR sample, for those candidate PNe/SNR sources, which may be associated with both PNe/SNR and HII regions or with

² <http://simbad.u-strasbg.fr/simbad/>

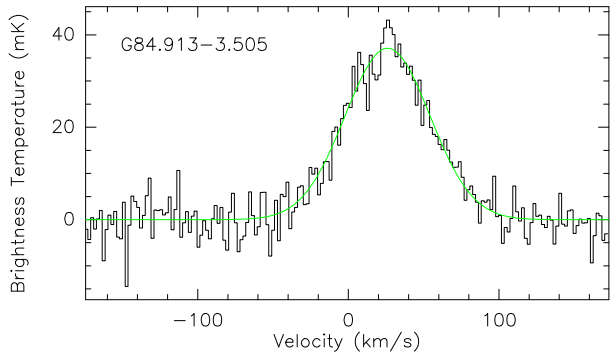


Figure 3. An example RRL from a PNe source with a line width of 58.7 km s^{-1} . The nominal position of this source is $\sim 68''$ away from the well-known PNe NGC7027. The spectra for the whole PNe sample can be found in the Appendix B.

PNe/SNR located near the edge of the detecting beam ($\sim 3'$ away), we remove them from the final HMSFR sample and denote them as “PNe?”/“SNR?” in Table 6 / 7. Notably, though spatially associated with PNe or SNR, the RRLs detected from those target positions may originate from HII regions along the LOS.

PNe usually has an expanding shell of ionized gas ejected from red giant stars. It is the main contamination of HII region samples traced by RRLs. RRLs from PNe usually have wider line width (typically $30 \sim 50 \text{ km s}^{-1}$) than those from HII regions (typical line width of $20 \sim 30 \text{ km s}^{-1}$) due to their expansion (see Garay et al. 1989; Balser et al. 1997). A typical RRL spectrum from PNe with a line width of $\sim 60 \text{ km s}^{-1}$ is shown in Figure 3. The existence of unknown PNe may cause a bias in the statistical analysis of the line width distribution for HII regions (see Section 4.2.2). There are 2 sources (G84.913–3.505; G85.946–3.488) which are explicitly associated with the well-built PNe NGC 7027, as well as 3 possible PNe sources. The full list of PNe candidates is given in Table 6.

SNRs are non-thermal radio sources, and generally have only weak RRLs with wide line width. Liu et al. (2019) suggested that the broad line width (mostly $> 50 \text{ km s}^{-1}$) of the RRLs toward SNRs implies high temperature or turbulent motions of the plasma. Former studies indicated that stimulated emission may be a possible origin for RRLs from SNRs (see Liu et al. 2019 and references therein). The potentially similar radio morphology of SNR and HII regions is the major confusion when disentangling these two samples (Anderson et al. 2017). There are 5 potential SNR candidates in our sample, all these sources are spatially associated with multiple sources thus no clear identifier can be designated. We list the potential SNR sources in Table 7. Figure 4 shows an example of RRL spectra from SNR.

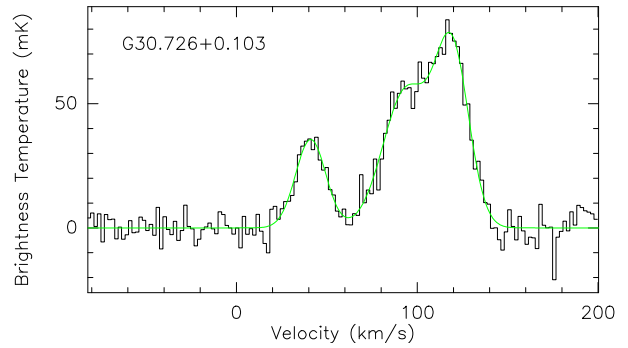


Figure 4. An example SNR source with three Gaussian RRL components. This source is $\sim 71''$ away from the previously identified SNR G030.3+00.7. The spectra for the whole SNR sample can be found in the Appendix C.

There is one potential SNR source (G28.532+0.129) which also exhibit methanol maser emission, however, it has a small spatial offset ($57.41''$) to a possible SNR source G28.5167+0.1333, and has a very wide RRL line width of 70.2 km s^{-1} , thus there may have both HMSFR and SNR sources along the LOS of this target. To minimize contamination, this source was excluded from the HMSFR sample and classified as a potential SNR.

4. DISCUSSION

4.1. Association and Correlation with Methanol Masers

In addition to our RRL emissions, there are 241 6.7-GHz class II methanol maser sources detected towards the same sample with TMRT (Yang et al. 2017, 2019) including one towards a potential SNR (G28.532+0.129; see Section 3.2). The majority of the maser sample (224/241) are close to the Galactic Plane ($|b| < 2^\circ$).

6.7 GHz methanol masers are believed to appear at an earlier stage of star formation, while HII regions typically exist at more evolved stages (see Section 2.1). Thus the association of 6.7 GHz methanol masers and RRLs would be helpful on discriminating HMSFRs at different evolutionary stages (Walsh et al. 1998; Jordan et al. 2017).

Our survey observed RRLs and methanol masers simultaneously with the same pointing positions, providing the most accurate results of cross-matching the signals. In addition, combining data from different surveys would bring systematic error in the cross-matching caused by inconsistent sensitivities and resolutions. Since we mainly focus on building up a cross-matched HMSFR sample, to reach higher reliability, we do not combine our data with the literature for the analysis in this paper. The 6.7-GHz class II methanol maser signal is observed and received by the 15th window in

our survey (see Table 1). Out of the 517 HMSFR sample with RRL detections, there are 103 (20.1%) sources associated with methanol masers, meanwhile, 43.2% (103/240) methanol maser sources (excluding one potential SNR) exhibit RRL emissions. The remaining 137 methanol maser sources without RRLs may correspond to a younger evolutionary stage compared to those with RRLs. We label the sources showing both emission features in Column (12) in Table 3. Notably, selecting targets from the point source catalog will bias the sample to include younger sources, and therefore may increase the number of sources associated with both RRL and maser. As a comparison, Anderson et al. (2011) found that only $\sim 10\%$ (46/448) of their HII region sample associated with methanol maser.

The correlation of LSR velocities between RRLs and methanol masers is shown in Figure 5. The majority of the associated RRL and methanol emissions seem to have fairly similar velocities, which intrinsically represent the systemic motion of the sources. As shown in Figure 5, there is one source (G25.395+0.033) which has a large offset between the V_{LSR} of RRL and maser. Due to the commonly extended morphology of HII regions, RRL and maser emissions detected from the same target position but with a large velocity offset may from different sources along the LOS, or different regions in the same extended cluster in our $\sim 3'$ beam.

As the processes of star formation at early stages are poorly understood, comparing the physical properties of HMSFR in different evolutionary stages will help us to study the formation and early evolution of massive star in such sources. We briefly discuss the spatial and intensity distributions of the three sub-sampled sources in the following sections, a more detailed discussion on their physical properties will be given in our future works.

4.1.1. Distance and Galactocentric Distance Distributions

Figure 6 shows the normalized distance and galactocentric distance (R_{Gal}) distributions of RRL-only sources, maser-only sources, and sources associated with both tracers. The average distances with standard deviations of the three samples are 5.62 ± 2.25 , 5.72 ± 3.69 kpc, and 6.63 ± 3.03 respectively. As shown in Figure 6a, the majority of our sources are located at $\lesssim 8$ kpc, and there is no significant difference between the distance distribution of the three samples. This is consistent with previous studies that HMSFRs at different stages are distributed similarly with distance (e.g. Urquhart et al. 2014).

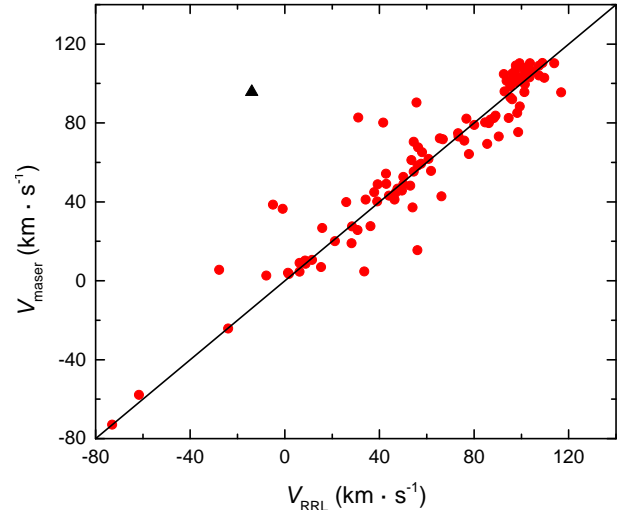


Figure 5. The correlation between radio V_{LSR} at peaks of RRL and methanol maser spectra. The solid line denotes where $V_{\text{maser}} = V_{\text{RRL}}$. There is one source marked with black triangles (G25.395+0.033) significantly departs from the rest of the sources.

The sources are more dispersed in the term of R_{Gal} . As shown in Figure 6b, although the three sub-samples have similar average R_{Gal} values (6.25 ± 2.09 , 6.95 ± 1.86 and 5.70 ± 1.77 kpc for RRL-only sources, maser-only sources, and sources with both RRL and maser, respectively), both RRL-only sources and sources associated with both tracers seem to be more adequate near the Galactic center. This can be explained by the fact that the thin gas at the outer Galaxy makes ionized hydrogen hard to be formed, and vice versa.

As illustrated by Figure 6b, three peaks can be seen in the distribution of R_{Gal} at ~ 3 –4, 6–7 and 8 kpc. The peak at 3–4 kpc for RRL-only sources and sources with both tracers may associate with the 4-kpc molecular ring (Dame et al. 2001). The peak at 6–7 kpc appears in the R_{Gal} distribution for all sources may coincident with the northern segment of Sagittarius arm. The sources at the 8-kpc peak may be mostly associated with the local SagittariusCarina arm.

4.1.2. RRL and Maser Line Intensity Distributions

Figure 7 presents the normalized distributions of peak line intensity corrected by distance of our samples, which is defined by the peak line intensity times the square of Bayesian distance (see Section 4.2.1 for more information). For the RRL sources, the peak line intensity used here are the main beam temperature (T_{mb}) of the RRLs. The RRL-only sources have a mean RRL intensity of 2.88 ± 0.70 mK kpc², which is lower than the mean intensity of 3.29 ± 0.60 mK kpc² of the sources associated

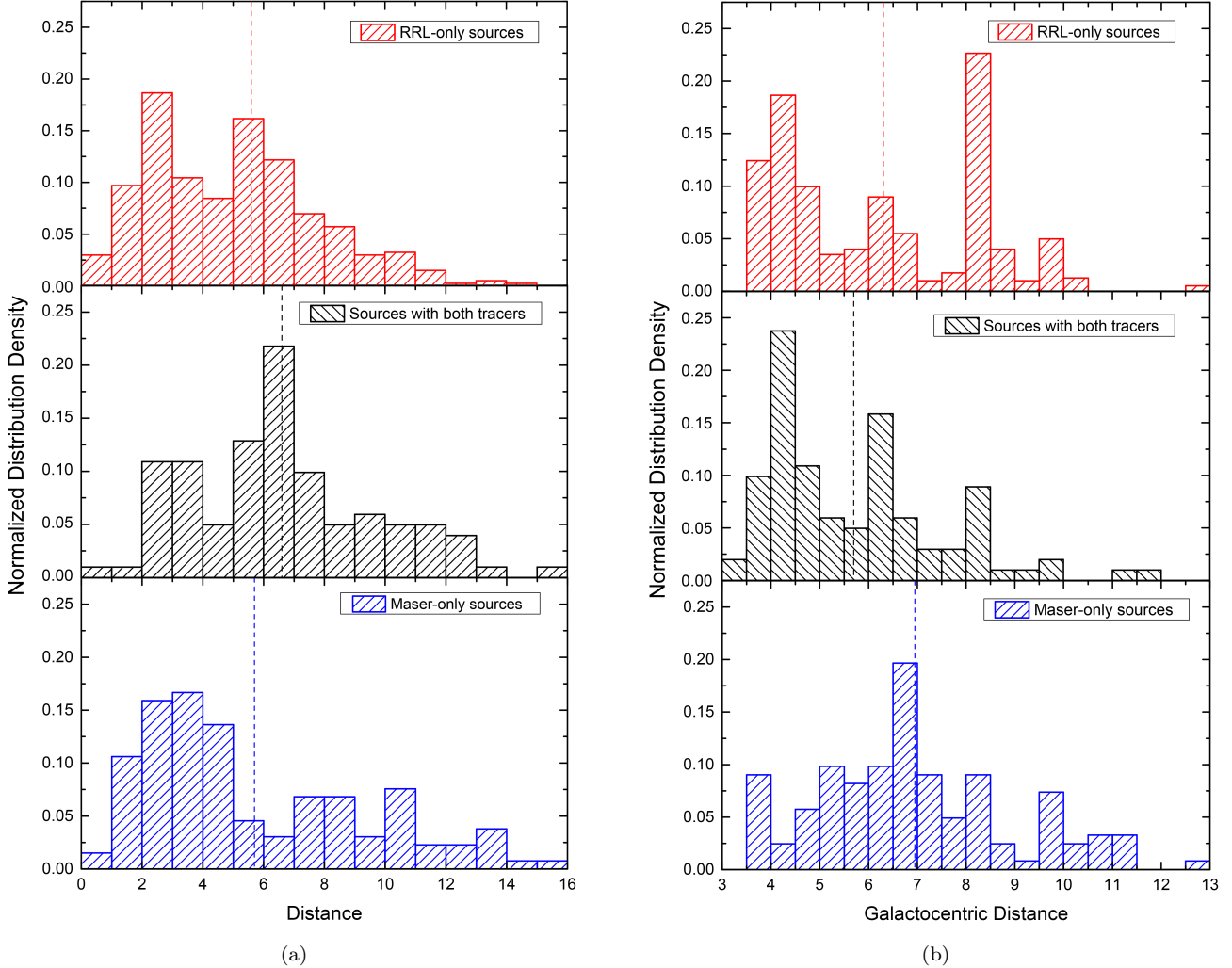


Figure 6. (a) Normalized distance distribution densities of the 414 RRL-only sources (upper panel), 103 sources with both RRL and maser (middle panel) and 137 maser-only sources (lower panel), as shown by the dotted lines, the average distances with standard deviations of the three samples are 5.62 ± 2.25 , 6.63 ± 3.03 and 5.72 ± 3.69 kpc, respectively. (b) Normalized galactocentric distance distribution densities of 414 RRL-only sources (upper panel), 103 sources associated with both tracers (middle panel) and 137 maser-only sources (lower panel), the dotted lines show the average galactocentric distances with standard deviations of 6.25 ± 2.09 , 5.70 ± 1.77 and 6.95 ± 1.86 kpc, respectively.

with both RRL and maser. Meanwhile, the maser-only sources and sources associated with both tracers have similar mean maser intensity of 1.95 ± 0.83 Jy kpc² and 2.11 ± 0.8 Jy kpc², respectively.

Urquhart et al. (2014) performed similar analyses and found that clumps with methanol maser sources have lower bolometric luminosity than those with HII regions. The authors suggested that this is because earlier stage massive stars with methanol masers are more heavily embedded than those at later stages without methanol maser. Although there is no significant difference between our maser line intensity distribution of maser-only and sources associated with both RRL and maser (Figure 7b), as shown in Figure 7a, RRL-

only sources have lower RRL line intensities than that of sources exhibiting methanol maser on average, and there is a lack of maser detection for RRL sources below 2.0 mK kpc². As illustrated by Ouyang et al. (2019), HII regions with methanol masers appear to have higher electron temperature and emission measure than those without, therefore methanol masers are more likely to be produced in regions with high gas densities and hence have a higher detection rate at more luminous HII regions.

4.2. Galactic Distribution

4.2.1. RRL Spatial Distribution

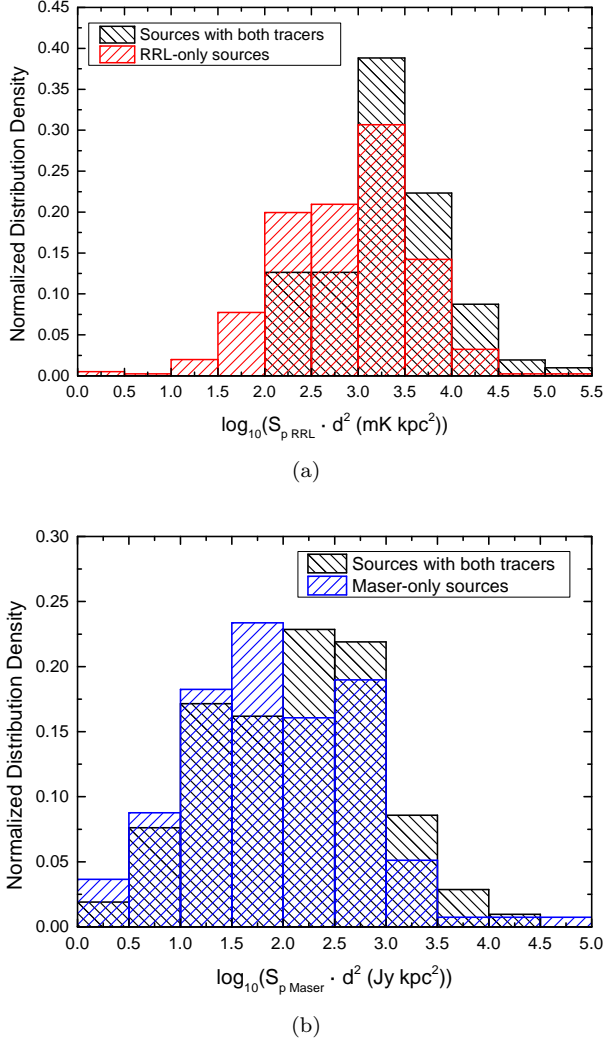


Figure 7. (a) The normalized distributions of RRL peak line intensity corrected by distance for the 414 RRL-only sources and 103 sources associated with both RRL and methanol maser, (b) the normalized distribution of maser peak line intensity corrected by distance for the 137 methanol-maser-only sources comparing to that of the 103 sources associated with both RRL and methanol maser.

Figure 8 represents the Galactic latitude and longitude distributions of the H-RRL-only sources, methanol-maser-only sources, sources associated with both tracers, and He RRL sources (see Section 4.3 for more details). As shown in this figure, a large fraction of the sources associated with both signals locate near the Galactic Plane, only 3 of them with a Galactic latitude larger than $\pm 2^\circ$, reflecting a sparse abundance in such regions.

The LSR velocities of the RRLs can be used to calculate the distance of its host HII regions using the

Bayesian distance calculator built by Reid et al. (2016)³. Reid et al. (2016) combines various types of distance information (spiral arm mode, kinematic distance, Galactic latitude, and parallax source) in a Bayesian approach, and fits the combined probability density function with multiple Gaussian components. The distance and error are estimated by the peak probability density and width of the Gaussian fitted component with maximum integrated probability density. The kinematic distances augmented by HI absorption spectra were used to resolve the near/far ambiguity for sources within the Solar circle. A user-adjustable prior probability (from 0 to 1) that the source is beyond the tangent point was set to the default value of 0.5. The result distances with error are presented in Column (9) and (10) in Table 3.

In Figure 9, we compare the velocity distribution along Galactic longitude of our HMSFRs to the longitude-velocity diagram retrieved from Vallée (2008). For sources exhibiting multiple RRL components with different peak velocities, we only use the peak velocity of the strongest component to do the analysis. As shown in this figure, most of the sources located in the first quadrant and our data align with the model curves well in the first and second quadrants.

4.2.2. Line Width Distribution

Figure 10 shows the RRL line width distribution of our HII region sample excluding those potential PNe, SNR and weak sources. These sources have an average line width with a standard deviation of $23.6 \pm 2.0 \text{ km s}^{-1}$, which is very close to that of the Anderson2014 catalog ($22.3 \pm 5.3 \text{ km s}^{-1}$).

Thermal broadened RRL has a line profile with an FWHM width proportional to $T^{1/2}\nu_o$ (Brocklehurst & Seaton 1972), where T is the temperature of the host HII region, ν_o is the rest central frequency. For a typical RRL-hosting source with $T \sim 5000$ to 13000 K across the Galaxy (Balsler et al. 2015), the corresponding thermal-broadened line width is ~ 15.3 to 24.6 km s^{-1} . In addition to thermal broadening, pressure broadening is also significant for RRLs at centimeter wavelengths (Keto et al. 2008). The ratio between pressure-broadened and thermal broadened line width is proportional to $n_e N^7$, where n_e is the electron density and N is the principal quantum number of the RRL transition (Brocklehurst & Seaton 1972; Griem 1974; Keto et al. 1995, 2008). As illustrated by Keto et al. (2008), since pressure broadening is proportional to the density of host HII region and less significant at high frequencies, comparing the line

³ <http://bessel.vlbi-astrometry.org/bayesian>

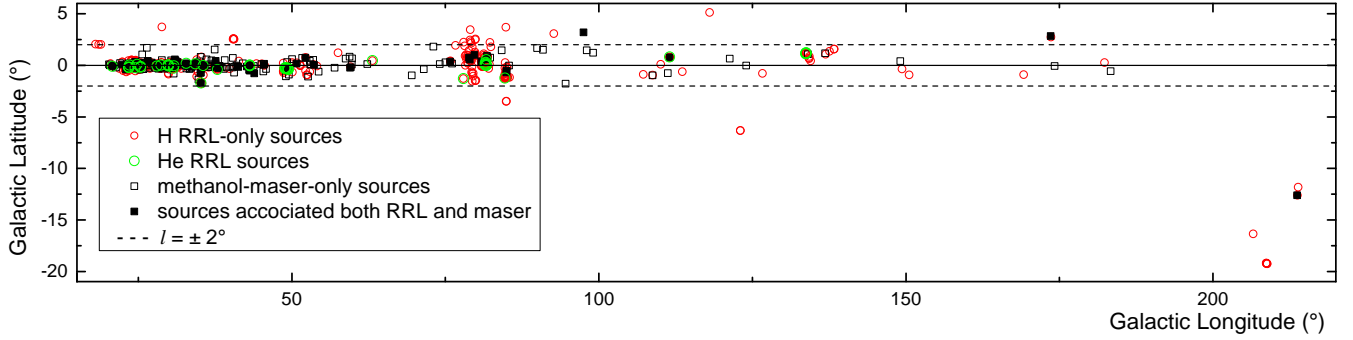


Figure 8. Positional distribution of sources with only H RRL, only methanol maser, He RRL, and both RRL and methanol maser. The dashed lines denote where $|b| = 2^\circ$.

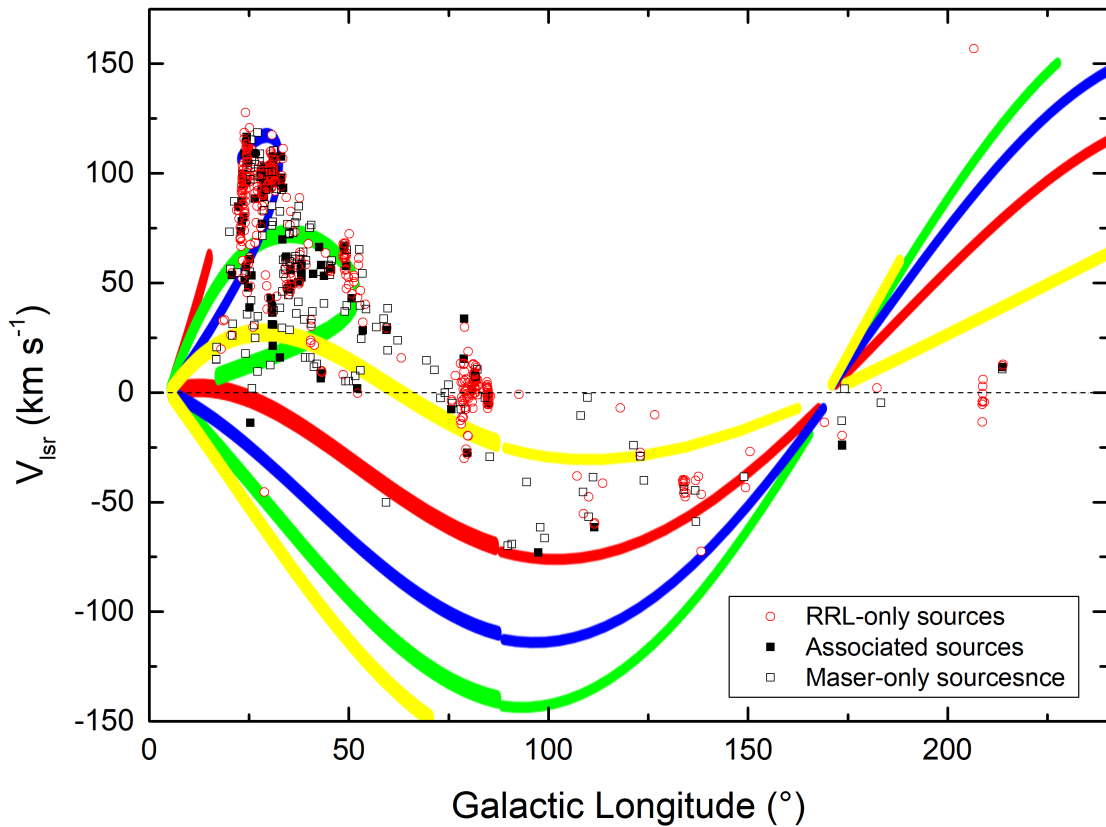


Figure 9. LSR velocities of HMSFRs along Galactic longitude. The background curves showing trajectories of spiral arms radial velocities as a function of Galactic longitude were taken from Vallée (2008). The spiral arms are colored by: red (NormaCygnus), blue (ScutumCrux); green (SagittariusCarina) and yellow (Perseus).

widths of RRLs measured with high-resolution interferometer in various wavelengths can be used to measure the electron density of the natal HII region.

RRLs with a line width narrower than 15 km s^{-1} are likely from comparably cold, sparse HII regions and are broadened purely by thermal, thus they can be used to probe the temperature of the host HII regions. There are 69 sources in our sample containing H RRLs with

a line width of $< 15 \text{ km s}^{-1}$, for thermally broadened RRL source with such narrow line width, the host HII regions have an upper limit to the temperature of $\lesssim 5000 \text{ K}$. According to Shaver (1970) and Shaver et al. (1979), RRLs with such narrow line width are from cold nebulae. Another possible explanation for the narrow line width is that the observed RRL line width is underestimated

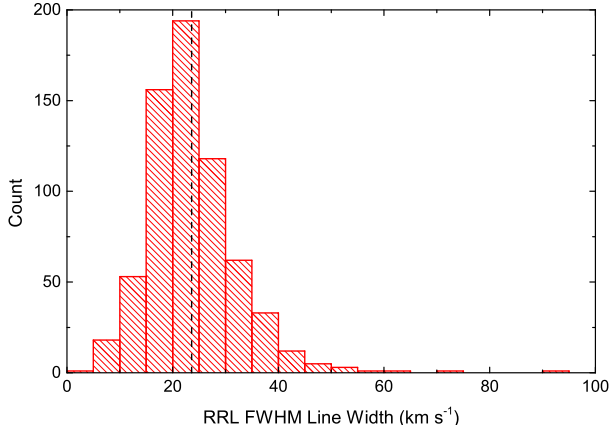


Figure 10. Line width distribution of the detected H RRL components. The dashed line denotes the mean value of 23.6 km s⁻¹

due to radiative transfer effect caused by strong free-free emission, which typically has a larger optical depth.

We detected 51 sources with a very broad line width (> 35 km s⁻¹). Out of these sources, 22 have a line width broader than 40 km s⁻¹. RRL with a line width > 40 km s⁻¹ may be very dense HII regions. For these RRLs, there may also exist large-scale motions around the central young stars (Sewilo et al. 2004; Ridge 2001; Reipurth & Bally 2001 and references therein) such as nebular expansion, rotation of the inner parts of the accretion disk, infall of matter, shocks, bipolar jets or photo evaporating flows.

Some of those broad line sources are possibly previously unknown PNe or SNR sources. As mentioned in Section 3.2, since PNe generally have larger line width due to expansion, their existence may affect the RRL line width distribution of our sample. For example, one of the sources, G28.393+0.085, with the widest line width in our sample was identified as a known HII region (G028.394+00.076) in Anderson et al. (2011). However, its RRL emission with extremely large line width is potentially from an unknown PNe or SNR source along the LOS. In addition, blended multiple RRL components with very close peak velocities may also cause confusion with a single wide line component.

4.3. Helium and Carbon RRLs

4.3.1. Helium RRL Detections

In addition to H RRLs, there are 49 sources also exhibit He RRLs. Their spatial distribution is shown in Figure 8. He RRLs are believed to have the same origin with H RRLs. The atomic heliums are ionized by the UV photons emitted by a central O6 or hotter star (Mezger 1978; Roshi et al. 2017). Since higher ionizing energy

is needed for He RRLs, they are generally from stars that are more massive than those emit H RRL only. He RRLs are usually weaker than H RRLs, they can only be detected from sources with strong H RRL intensities. In our sample, the mean peak temperature of H RRL from the sources with He RRL emissions is 374.7 mK, which is ~ 8 times brighter than those without He RRL detections. The detected He RRLs have a mean peak temperature of 31.6 mK and an average value of $T_{p\text{He}}/T_{p\text{H}} \sim 0.1$, where $T_{p\text{He}}$ and $T_{p\text{H}}$ denote the peak temperatures of He and H RRLs. Due to sensitivity limitation, He RRLs with peak temperature lower than ~ 7 mK are below our detection threshold, this results in a lower limit to the $T_{p\text{H}}$ of 70 mK for He RRL to be detected. Figure 11 shows the plot between $T_{p\text{He}}$ and $T_{p\text{H}}$. For sources without He RRL detections, the expected $T_{p\text{He}}$ values are calculated by multiplying their $T_{p\text{H}}$ by 0.1. There are 76 sources which have an H RRL peak temperature above 70 mK (black dots above the red dashed line in Figure 11) but had no He RRL detections, showing a low abundance of He⁺.

We averaged over the H-RRL-only sources with $T_{p\text{H}}$ above and below 70 mK, as shown in Figure 12. After averaging, He RRLs can be seen with a $S_{i\text{He}}$ to $S_{i\text{H}}$ ratio of ~ 0.01 and ~ 0.02 for sources above and below 70 mK, respectively, where $S_{i\text{He}}$ and $S_{i\text{H}}$ denote the integrated intensities of He and H RRLs. These values are much lower than the mean $S_{i\text{He}}$ to $S_{i\text{H}}$ ratio of 0.06 for sources with He RRL detections. This fact may suggest that in addition to the selecting effect caused by the sensitivity limit, the non-detections of He RRLs for the H-RRL-only sources may be mostly originated from the low abundance of He⁺. Those sources are possibly being ionized by a less massive, later OB-type star. That is, helium is under ionized with respect to hydrogen.

4.3.2. Distance and Galactocentric Distance Distribution

Figure 13 shows the normalized distance distribution of the 76 H-RRL-only sources with $T_{p\text{H}} > 70$ mK and 380 sources (excluding the weak sources, and for multi-component sources, only the strongest emission were taken into consideration.) with $T_{p\text{H}} < 70$ mK comparing to the 49 sources with He RRL. No significant difference in the distance distributions were found for the two sub-samples in this figure. This fact may support the argument that the non-detections of He RRLs are mainly caused by the low abundance of He⁺ rather than sensitivity limit caused by distance.

Figure 14 shows the normalized R_{Gal} distribution density of the 49 He RRL sources and the 76 H-RRL-only sources with $T_{p\text{H}}$ above 70 mK. As shown in this figure,

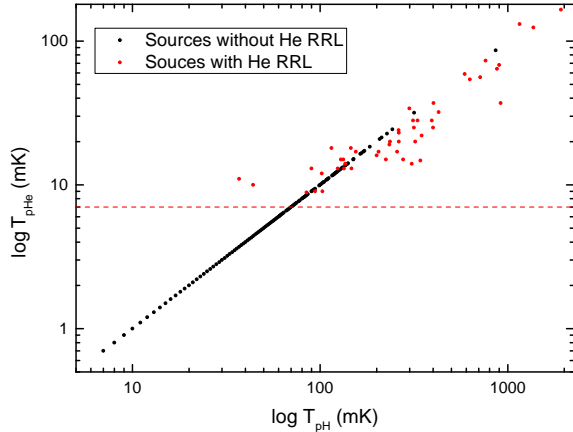


Figure 11. The peak temperature distribution of He RRLs versus the peak temperature of H RRLs. The red and black dots represent sources with and without He RRL detections. For sources without He RRL detections, the expected $T_{p\text{He}}$ values are calculated by multiplying their $T_{p\text{H}}$ by the mean $T_{p\text{He}}$ to $T_{p\text{H}}$ ratio of 0.1. The dashed red line denotes the detection threshold of 7 mK. H-RRL-only sources with $T_{p\text{H}} > 70$ mK are likely to have no or very weak He RRL emissions.

sources without He RRL emissions locate nearer to the Galactic center than those with He RRLs on average. Under the above assumption that He RRL sources are being ionized by a more massive star with respect to those without He RRL, we suggest that more massive SFRs locate at longer distances on average. This is contradicting to previous studies that due to higher gas density, there is a concentration of mass in the inner Galaxy (e.g., [Green & McClure-Griffiths 2011](#); [Casasus et al. 2000](#); [Lépine et al. 2011](#)). A more plausible explanation for the lower abundance of ionized He is line-blanketing effect caused by higher metallicity in such regions. There is a known negative metallicity radial gradient along the Galactic disk ([Henry & Worthey 1999](#)), the higher metal content in the atmosphere of OB-type stars near the Galactic Center will cause line-blanketing and reduce the number of He-ionizing photons that escape the star. This may result in a lower abundance of ionized He in such regions. Nevertheless, both [Figures 13](#) and [14](#) may suffer from statistical bias due to limited sample size.

4.3.3. He^+ Abundance along the Galactic Plane

H and He RRLs with high principal quantum numbers in the radio act similarly, so their line intensity ratio y^+ can be used to diagnose the abundance ratio between $^4\text{He}^+$ and H^+ ([Wenger et al. 2013](#); [Balsler 2006](#)). y^+ is defined as the following:

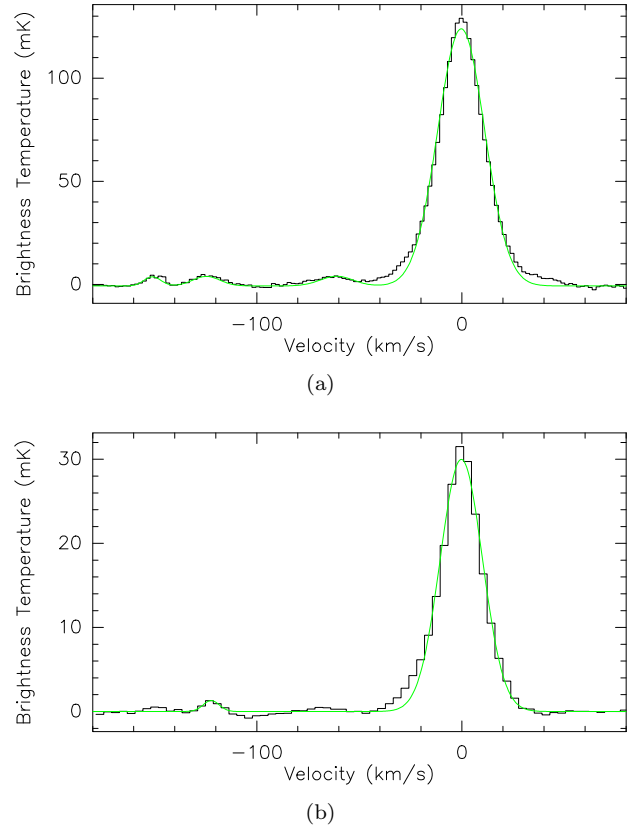
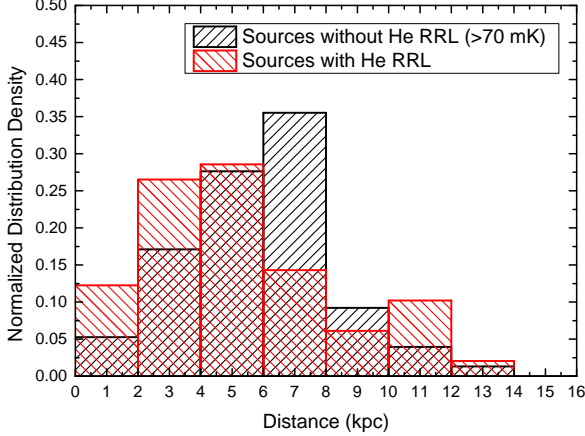


Figure 12. The averaged spectra over sources without He RRL detection with (a) $T_{p\text{H}} > 70$ mK and (b) $T_{p\text{H}} < 70$ mK. The peak velocity of each individual spectrum was aligned and set to zero. He RRLs in (a) and (b) appear at -122 km s^{-1} . The C RRL (-149 km s^{-1}) and $\text{H}\beta$ line (-60 km s^{-1}) can also be seen clearly in (a).

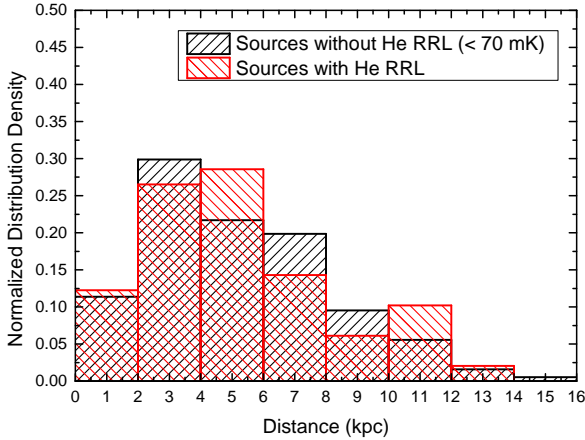
$$y^+ = \frac{T_{p\text{He}^+} \Delta\nu_{\text{He}^+}}{T_{p\text{H}^+} \Delta\nu_{\text{H}^+}} \quad (1)$$

where $T_{p\text{He}^+}$ and $T_{p\text{H}^+}$ are the peak line temperatures of He and H RRLs, $\Delta\nu_{\text{He}^+}$ and $\Delta\nu_{\text{H}^+}$ are the line widths of them, respectively.

The distribution of y^+ values along the Galactic Plane for the sources exhibiting He RRLs is presented in [Figure 15](#). Our sample has a mean y^+ value with a standard deviation of 0.062 ± 0.029 , this value is similar to that of the [Anderson2014](#) catalog (0.068 ± 0.023) measured in [Wenger et al. \(2013\)](#). Our sample shows no significant trend on y^+ with R_{Gal} , as presented by the black fitting line in [Figure 15](#), a small positive slope of 0.002 ± 0.015 is derived for the sources. There is a very low correlation coefficient of ~ 0.09 between y^+ and R_{Gal} , and a large standard error of ± 0.015 to the fitting line slope, both showing weak dependence of y^+ on R_{Gal} . This is consistent with earlier studies that y^+ has a negative or no obvious gradient with R_{Gal} through our Galaxy (see



(a)



(b)

Figure 13. The distance distribution of (a) 76 H-RRL-only sources with $T_{pH} > 70$ mK and (b) 380 sources with $T_{pH} < 70$ mK with respect to the distribution of 49 He RRL sources. There is a slight higher distance distribution on the H-RRL-only sources in (a) and no significant difference found in (b).

Balsler et al. 2001 for a review). A weak increasing trend was also found on y^+ ($y^+ = 0.0035 \pm 0.0016$ kpc $^{-1}$) in Wenger et al. (2013), however, they pointed out that this result only weakly constrains the actual y^+ gradient due to the large uncertainties in their data. Due to the limited sample size, our analysis may also suffer from statistical bias.

There are two sources with prominently high y^+ values (> 0.15) (G23.563+0.008 and G84.722-1.248; see Figure 15), as concluded by Balsler et al. (2001), possible origins for the high y^+ value are mass loss of helium near the surface of the massive star or overestimated abundance due to the radiative transfer effect.

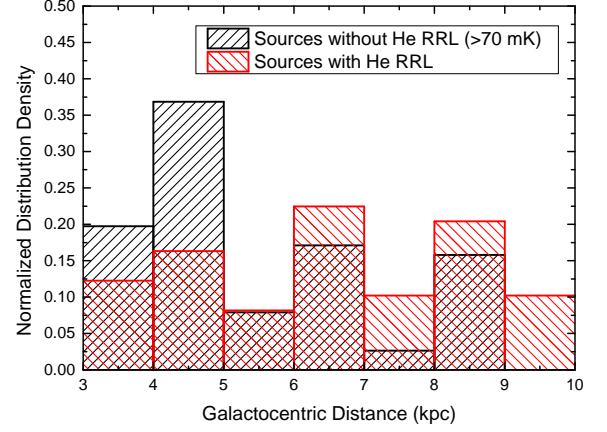


Figure 14. Normalized galactocentric distance distribution density of the 49 He sources and the 76 H-RRL-only sources with T_{pH} above 70 mK.

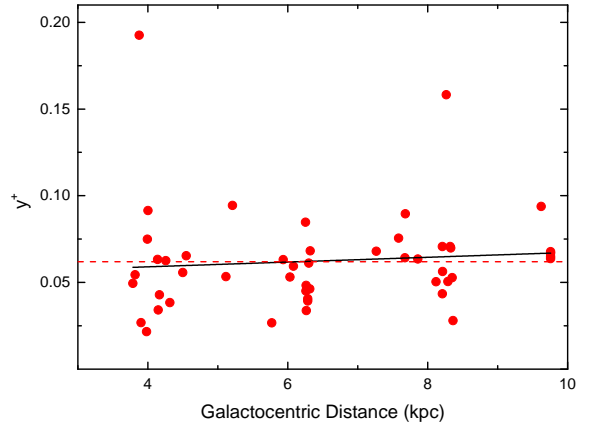


Figure 15. The distribution of y^+ values along the galactocentric distance for the sources which exhibit He RRLs. The solid black line shows a linear fit to the sample. The dashed red line mark the location of the mean y^+ of 0.062 ± 0.029 .

4.3.4. MIR Color Distribution

Due to the emission from the dust heated by the central star, one would expect higher luminosities at longer MIR wavelength from more massive SFRs, thus there may exist a difference between the color-color distribution of HII regions with different masses of their exciting stars. Figure 16 shows the *WISE* [12] – [22] vs. [3.4] – [4.6] and [4.6] – [12] vs. [3.4] – [4.6] color distributions of sources with and without He RRL detections (above 70 mK). However, there is no significant separation found between the color distributions of these two sub-samples. This may suggest that *WISE* colors are insensitive to mass variation of UCHII regions.

4.3.5. Carbon RRLs

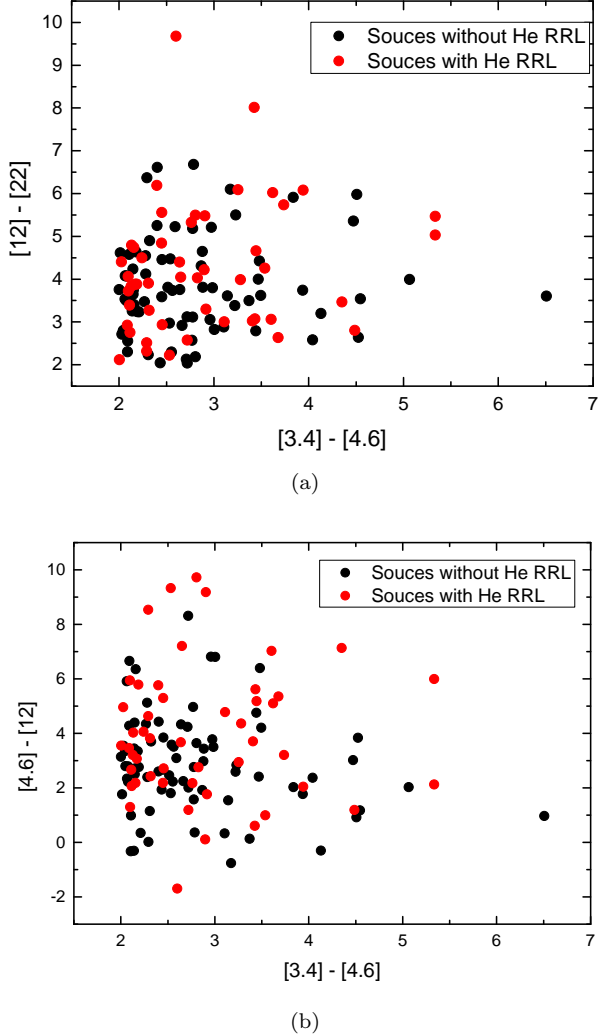


Figure 16. The *All-WISE* (a) $[12] - [22]$ vs. $[3.4] - [4.6]$ and (b) $[4.6] - [12]$ vs. $[3.4] - [4.6]$ colors of sources with and without He RRL emission. For the He-undetected sources, only those with T_{pH} above 70 mK are included in this figure. Both (a) and (b) show no significant difference in the color distribution of the two sub-samples.

Carbon RRLs are from cooler gas in photo-dissociation regions (PDRs) or diffuse gas ionized by the interstellar UV radiation (see [Alves et al. 2015](#) and references therein). For a target position with both H and C RRLs, if the C RRL is emitted from a cold gas with a different velocity to the HII region, it can have a shifted velocity offset with respect to the H RRLs ([Alves et al. 2012](#)). There are 23 sources showing C RRL in our sample, 3 of them are from the nearby Orion Molecular Cloud Complex (G208.894–19.313; G213.706–12.602; G213.885–11.832). The line properties of the 23 C RRLs are presented in Table 5.

C RRLs are essential to the studies of morphology and physical properties of its host PDR (e.g., [Roshi & Anantharamaiah 2001](#); [Roshi et al. 2002](#); [Wenger et al. 2013](#)). For example, the non-thermal component of the carbon RRL line width can be used to diagnose the magnetic field in the host PDR ([Roshi 2007](#); [Balsler et al. 2016](#)). For a thermally broadened C RRL, assuming a typical PDR temperature of $\sim 10^3$ K, a line width of $\sim \text{km s}^{-1}$ is expected. However, the C RRLs in our sample have an average line width of 8.9 km s^{-1} . The large average line width of C RRLs may indicate that there may exist non-thermal turbulence in the PDRs in our sample ([Roshi 2007](#) and [Barrett 1964](#)).

5. SUMMARY

(1) Using the TMRT, we performed a Galactic RRL survey in C band toward 3348 targets, selected from the *WISE* point source catalog. Excluding 5 potential PNe and 5 potential SNR candidates, we built a sample of 517 HMSFRs traced by RRL. The peak flux densities of the detected hydrogen RRLs are in a range of ~ 10 to 1900 mK. Though the majority of the sources have a line width within $15 \sim 35 \text{ km s}^{-1}$, there are 82 of them show very narrow line width characteristic and 30 of them have line width larger than 35 km s^{-1} . Our sample further expanded the HII region sample on the basis of previous surveys.

(2) Within the detected HII region sample, 103 sources also harbor 6.7 GHz methanol masers emissions. Combining the sources traced by RRL and/or maser, we built up a sample of 654 HMSFRs, providing fundamental information to study the high-mass star formation evolutionary stages. According to the argument that methanol maser appears earlier than the formation of HII region, our sources may be associated with HMSFR at various star-forming sequences. By comparing the physical properties of the RRL-only sources, maser-only sources and sources associated with both tracers, we found no significant difference in distance and R_{Gal} distribution of the three sub-samples. A slightly higher maser association rate was found for more luminous RRL sources.

(3) In addition to H RRL, we also detected He RRLs from 49 sources which may associate with more massive HMSFRs, no significant gradient on the He/H abundance along the galactocentric distance was found from the 49 He RRL sources.

(4) A sample of 23 C RRLs were also built in this survey, which provides a promising sample for future studies on the physical properties of PDRs surrounding HII regions, the wide average line width of C RRLs may

indicate non-thermal turbulence in their host PDRs.

ACKNOWLEDGEMENT

We are thankful for the assistance from the operators of the TMRT during the observations, the funding and support from China Scholarship Council (CSC) (File No.201704910999), Science and Technology Facilities Council (STFC) and the University of Manch-

ester. This work was supported by the National Natural Science Foundation of China (11590781, 11590783, 11590784 and 11873002), and Guangdong Province Universities and Colleges Pearl River Scholar Funded Scheme (2019).

Software: GILDAS/CLASS(Pety 2005; Gildas Team 2013)

REFERENCES

- Alves, M. I. R., Calabretta, M., Davies, R. D., et al. 2015, MNRAS, 450, 2025, doi: [10.1093/mnras/stv751](https://doi.org/10.1093/mnras/stv751)
- Alves, M. I. R., Davies, R. D., Dickinson, C., et al. 2012, MNRAS, 422, 2429, doi: [10.1111/j.1365-2966.2012.20796.x](https://doi.org/10.1111/j.1365-2966.2012.20796.x)
- Anderson, L. D. 2010, PhD thesis, Boston University
- Anderson, L. D., & Bania, T. M. 2009, ApJ, 690, 706, doi: [10.1088/0004-637X/690/1/706](https://doi.org/10.1088/0004-637X/690/1/706)
- Anderson, L. D., Bania, T. M., Balsler, D. S., et al. 2014, ApJS, 212, 1, doi: [10.1088/0067-0049/212/1/1](https://doi.org/10.1088/0067-0049/212/1/1)
- Anderson, L. D., Bania, T. M., Balsler, D. S., & Rood, R. T. 2011, ApJS, 194, 32, doi: [10.1088/0067-0049/194/2/32](https://doi.org/10.1088/0067-0049/194/2/32)
- Anderson, L. D., Wang, Y., Bihr, S., et al. 2017, A&A, 605, A58, doi: [10.1051/0004-6361/201731019](https://doi.org/10.1051/0004-6361/201731019)
- Balsler, D. S. 2006, AJ, 132, 2326, doi: [10.1086/508515](https://doi.org/10.1086/508515)
- Balsler, D. S., Anish Roshi, D., Jeyakumar, S., et al. 2016, ApJ, 816, 22, doi: [10.3847/0004-637X/816/1/22](https://doi.org/10.3847/0004-637X/816/1/22)
- Balsler, D. S., Bania, T. M., Rood, R. T., & Wilson, T. L. 1997, ApJ, 483, 320, doi: [10.1086/304248](https://doi.org/10.1086/304248)
- Balsler, D. S., Goss, W. M., & De Pree, C. G. 2001, AJ, 121, 371, doi: [10.1086/318028](https://doi.org/10.1086/318028)
- Balsler, D. S., Rood, R. T., Bania, T. M., & Anderson, L. D. 2011, ApJ, 738, 27, doi: [10.1088/0004-637X/738/1/27](https://doi.org/10.1088/0004-637X/738/1/27)
- Balsler, D. S., Wenger, T. V., Anderson, L. D., & Bania, T. M. 2015, ApJ, 806, 199, doi: [10.1088/0004-637X/806/2/199](https://doi.org/10.1088/0004-637X/806/2/199)
- Barrett, A. H. 1964, Nature, 202, 475, doi: [10.1038/202475a0](https://doi.org/10.1038/202475a0)
- Bernasconi, P. A., & Maeder, A. 1996, A&A, 307, 829
- Breen, S. L., Fuller, G. A., Caswell, J. L., et al. 2015, MNRAS, 450, 4109, doi: [10.1093/mnras/stv847](https://doi.org/10.1093/mnras/stv847)
- Brocklehurst, M., & Seaton, M. J. 1972, MNRAS, 157, 179, doi: [10.1093/mnras/157.2.179](https://doi.org/10.1093/mnras/157.2.179)
- Bussa, S., & VEGAS Development Team. 2012, in American Astronomical Society Meeting Abstracts, Vol. 219, American Astronomical Society Meeting Abstracts #219, 446.10
- Casassus, S., Bronfman, L., May, J., & Nyman, L. Å. 2000, A&A, 358, 514. <https://arxiv.org/abs/astro-ph/9912430>
- Caswell, J. L., & Haynes, R. F. 1987, A&A, 171, 261
- Caswell, J. L., Fuller, G. A., Green, J. A., et al. 2010, MNRAS, 404, 1029, doi: [10.1111/j.1365-2966.2010.16339.x](https://doi.org/10.1111/j.1365-2966.2010.16339.x)
- . 2011, MNRAS, 417, 1964, doi: [10.1111/j.1365-2966.2011.19383.x](https://doi.org/10.1111/j.1365-2966.2011.19383.x)
- Churchwell, E. 2002, ARA&A, 40, 27, doi: [10.1146/annurev.astro.40.060401.093845](https://doi.org/10.1146/annurev.astro.40.060401.093845)
- Dame, T. M., Hartmann, D., & Thaddeus, P. 2001, ApJ, 547, 792, doi: [10.1086/318388](https://doi.org/10.1086/318388)
- Downes, D., Wilson, T. L., Bieging, J., & Wink, J. 1980, A&AS, 40, 379
- Ellingsen, S. P. 2006, ApJ, 638, 241, doi: [10.1086/498673](https://doi.org/10.1086/498673)
- Garay, G., Gathier, R., & Rodriguez, L. F. 1989, A&A, 215, 101
- Gildas Team. 2013, GILDAS: Grenoble Image and Line Data Analysis Software. <http://ascl.net/1305.010>
- Green, J. A., & McClure-Griffiths, N. M. 2011, MNRAS, 417, 2500, doi: [10.1111/j.1365-2966.2011.19418.x](https://doi.org/10.1111/j.1365-2966.2011.19418.x)
- Green, J. A., Caswell, J. L., Fuller, G. A., et al. 2010, MNRAS, 409, 913, doi: [10.1111/j.1365-2966.2010.17376.x](https://doi.org/10.1111/j.1365-2966.2010.17376.x)
- . 2012, MNRAS, 420, 3108, doi: [10.1111/j.1365-2966.2011.20229.x](https://doi.org/10.1111/j.1365-2966.2011.20229.x)
- Griem, H. R. 1974, Spectral line broadening by plasmas
- Gum, C. S. 1955, MmRAS, 67, 155
- Henry, R. B. C., & Worthey, G. 1999, PASP, 111, 919, doi: [10.1086/316403](https://doi.org/10.1086/316403)
- Hoglund, B., & Mezger, P. G. 1965, Science, 150, 339, doi: [10.1126/science.150.3694.339](https://doi.org/10.1126/science.150.3694.339)
- Hou, L. G., & Han, J. L. 2015, MNRAS, 454, 626, doi: [10.1093/mnras/stv1904](https://doi.org/10.1093/mnras/stv1904)
- Hu, B., Menten, K. M., Wu, Y., et al. 2016, ApJ, 833, 18, doi: [10.3847/0004-637X/833/1/18](https://doi.org/10.3847/0004-637X/833/1/18)
- Jordan, C. H., Walsh, A. J., Breen, S. L., et al. 2017, MNRAS, 471, 3915, doi: [10.1093/mnras/stx1776](https://doi.org/10.1093/mnras/stx1776)

- Keto, E., Zhang, Q., & Kurtz, S. 2008, *ApJ*, 672, 423, doi: [10.1086/522570](https://doi.org/10.1086/522570)
- Keto, E. R., Welch, W. J., Reid, M. J., & Ho, P. T. P. 1995, *ApJ*, 444, 765, doi: [10.1086/175649](https://doi.org/10.1086/175649)
- Lépine, J. R. D., Cruz, P., Scarano, S., J., et al. 2011, *MNRAS*, 417, 698, doi: [10.1111/j.1365-2966.2011.19314.x](https://doi.org/10.1111/j.1365-2966.2011.19314.x)
- Liu, B., Anderson, L. D., McIntyre, T., et al. 2019, *ApJS*, 240, 14, doi: [10.3847/1538-4365/aaef8e](https://doi.org/10.3847/1538-4365/aaef8e)
- Liu, B., McIntyre, T., Terzian, Y., et al. 2013, *AJ*, 146, 80, doi: [10.1088/0004-6256/146/4/80](https://doi.org/10.1088/0004-6256/146/4/80)
- Lockman, F. J. 1989, *ApJS*, 71, 469, doi: [10.1086/191383](https://doi.org/10.1086/191383)
- Mezger, P. G., & Hoglund, B. 1967, *ApJ*, 147, 490, doi: [10.1086/149031](https://doi.org/10.1086/149031)
- Mezger, P. O. 1978, *A&A*, 70, 565
- Minier, V., Ellingsen, S. P., Norris, R. P., & Booth, R. S. 2003, *A&A*, 403, 1095, doi: [10.1051/0004-6361:20030465](https://doi.org/10.1051/0004-6361:20030465)
- Oey, M. S., & Kennicutt, R. C., J. 1997, *MNRAS*, 291, 827, doi: [10.1093/mnras/291.4.827](https://doi.org/10.1093/mnras/291.4.827)
- Ouyang, X.-J., Chen, X., Shen, Z.-Q., et al. 2019, *ApJS*, 245, 12, doi: [10.3847/1538-4365/ab4db2](https://doi.org/10.3847/1538-4365/ab4db2)
- Pety, J. 2005, in *SF2A-2005: Semaine de l'Astrophysique Française*, ed. F. Casoli, T. Contini, J. M. Hameury, & L. Pagani, 721
- Quiroza, C., Rood, R. T., Bania, T. M., Balser, D. S., & Maciel, W. J. 2006, *ApJ*, 653, 1226, doi: [10.1086/508803](https://doi.org/10.1086/508803)
- Reid, M. J., Dame, T. M., Menten, K. M., & Brunthaler, A. 2016, *ApJ*, 823, 77, doi: [10.3847/0004-637X/823/2/77](https://doi.org/10.3847/0004-637X/823/2/77)
- Reifenstein, E. C., Wilson, T. L., Burke, B. F., Mezger, P. G., & Altenhoff, W. J. 1970, *A&A*, 4, 357
- Reipurth, B., & Bally, J. 2001, *ARA&A*, 39, 403, doi: [10.1146/annurev.astro.39.1.403](https://doi.org/10.1146/annurev.astro.39.1.403)
- Ridge, N. A. 2001, PhD thesis, FCRAO, 619 Lederle GRC, University of Massachusetts, Amherst, MA 01003, USA
- Rodgers, A. W., Campbell, C. T., & Whiteoak, J. B. 1960, *MNRAS*, 121, 103, doi: [10.1093/mnras/121.1.103](https://doi.org/10.1093/mnras/121.1.103)
- Roshi, D. A. 2007, *ApJL*, 658, L41, doi: [10.1086/513465](https://doi.org/10.1086/513465)
- Roshi, D. A., & Anantharamaiah, K. R. 2001, *ApJ*, 557, 226, doi: [10.1086/321586](https://doi.org/10.1086/321586)
- Roshi, D. A., Churchwell, E., & Anderson, L. D. 2017, *ApJ*, 838, 144, doi: [10.3847/1538-4357/aa662b](https://doi.org/10.3847/1538-4357/aa662b)
- Roshi, D. A., Kantharia, N. G., & Anantharamaiah, K. R. 2002, *A&A*, 391, 1097, doi: [10.1051/0004-6361:20020899](https://doi.org/10.1051/0004-6361:20020899)
- Sewilo, M., Churchwell, E., Kurtz, S., Goss, W. M., & Hofner, P. 2004, *ApJ*, 605, 285, doi: [10.1086/382268](https://doi.org/10.1086/382268)
- Sharpless, S. 1953, *ApJ*, 118, 362, doi: [10.1086/145765](https://doi.org/10.1086/145765)
- . 1959, *ApJS*, 4, 257, doi: [10.1086/190049](https://doi.org/10.1086/190049)
- Shaver, P. A. 1970, *Astrophys. Lett.*, 5, 167
- Shaver, P. A., McGee, R. X., Newton, L. M., Danks, A. C., & Pottasch, S. R. 1983, *MNRAS*, 204, 53, doi: [10.1093/mnras/204.1.53](https://doi.org/10.1093/mnras/204.1.53)
- Shaver, P. A., McGee, R. X., & Pottasch, S. R. 1979, *Nature*, 280, 476, doi: [10.1038/280476a0](https://doi.org/10.1038/280476a0)
- Tan, J. C., Beltrán, M. T., Caselli, P., et al. 2014, in *Protostars and Planets VI*, ed. H. Beuther, R. S. Klessen, C. P. Dullemond, & T. Henning, 149
- Urquhart, J. S., Moore, T. J. T., Csengeri, T., et al. 2014, *MNRAS*, 443, 1555, doi: [10.1093/mnras/stu1207](https://doi.org/10.1093/mnras/stu1207)
- Vallée, J. P. 2008, *AJ*, 135, 1301, doi: [10.1088/0004-6256/135/4/1301](https://doi.org/10.1088/0004-6256/135/4/1301)
- Walsh, A. J., Burton, M. G., Hyland, A. R., & Robinson, G. 1998, *MNRAS*, 301, 640, doi: [10.1046/j.1365-8711.1998.02014.x](https://doi.org/10.1046/j.1365-8711.1998.02014.x)
- Wenger, T. V., Bania, T. M., Balser, D. S., & Anderson, L. D. 2013, *ApJ*, 764, 34, doi: [10.1088/0004-637X/764/1/34](https://doi.org/10.1088/0004-637X/764/1/34)
- Wilson, T. L., Mezger, P. G., Gardner, F. F., & Milne, D. K. 1970, *A&A*, 6, 364
- Wink, J. E., Wilson, T. L., & Bieging, J. H. 1983, *A&A*, 127, 211
- Xu, Y., Li, J. J., Hachisuka, K., et al. 2008, *A&A*, 485, 729, doi: [10.1051/0004-6361:200809472](https://doi.org/10.1051/0004-6361:200809472)
- Yang, K., Chen, X., Shen, Z.-Q., et al. 2017, *ApJ*, 846, 160, doi: [10.3847/1538-4357/aa8668](https://doi.org/10.3847/1538-4357/aa8668)
- . 2019, *ApJS*, 241, 18, doi: [10.3847/1538-4365/ab06fb](https://doi.org/10.3847/1538-4365/ab06fb)
- Zavagno, A., Pomarès, M., Deharveng, L., et al. 2007, *A&A*, 472, 835, doi: [10.1051/0004-6361:20077474](https://doi.org/10.1051/0004-6361:20077474)
- Zinnecker, H., & Yorke, H. W. 2007, *ARA&A*, 45, 481, doi: [10.1146/annurev.astro.44.051905.092549](https://doi.org/10.1146/annurev.astro.44.051905.092549)

Table 3. Characteristics of the Hydrogen RRL emission sample.

Name	R.A.	Decl.	Epoch	T_b	S_i	ΔV	ν_p	d	σ_d	Notes	Maser	Other Name(s)
(1)	(2)	(3)	(4)	(5)	(6)	(7)	(8)	(9)	(10)	(11)	(12)	(13)
($^{\circ}$, $'$)	(h m s)	($^{\circ}$ $'$ $''$)	(dd/mm/yy)	(mK)	(K km s $^{-1}$)	(km s $^{-1}$)	(km s $^{-1}$)	(kpc)	(kpc)			
G18.059+2.035	18:16:27.60	-12:14:45.7	22/04/16	26	0.53(0.05)	19.4(2.0)	19.7(0.8)	1.69	0.24			(K) G018.426+01.922
G18.559+2.029	18:17:26.97	-11:48:32.0	15/12/17	49	1.26(0.05)	24.4(1.1)	32.7(0.5)	1.77	0.26			(K) G018.426+01.922 / IRAS 18146-1148
G18.915+2.027	18:18:08.75	-11:29:45.2	15/12/17	31	0.42(0.04)	12.7(1.3)	33.1(0.5)	1.77	0.26			(K) G018.426+01.922 / IRAS 18153-1131
G20.495+0.157	18:27:54.06	-10:58:37.3	04/07/16	52	1.10(0.04)	19.7(0.9)	26.1(0.4)	14.01	0.31			(K) G020.481+00.168
G20.749-0.112	18:29:21.28	-10:52:38.5	04/07/16	263	7.54(0.06)	26.9(0.2)	54.5(0.1)	3.46	0.20			(K) G020.728-00.105 / K _{es} 68
G20.762-0.064	18:29:12.19	-10:50:36.0	04/07/16	243	5.52(0.06)	21.3(0.2)	53.5(0.1)	3.45	0.20		yes	(K) G020.728-00.105 / K _{es} 68
G21.919-0.324	18:32:19.23	-09:56:19.9	04/07/16	41	0.85(0.05)	19.5(1.4)	83.2(0.6)	5.27	0.32			(K) G021.884-00.318 / IRAS 18294-0959
G22.355+0.066	18:31:44.05	-09:22:17.3	15/07/16	39	0.80(0.05)	19.1(1.3)	84.7(0.6)	5.41	0.37		yes	(K) G022.357+00.064
G22.396+0.334	18:30:50.75	-09:12:39.8	15/07/16	21	0.27(0.03)	12.1(1.6)	82.9(0.7)	5.38	0.40			(C) G022.424+00.337

NOTE—Properties of the H RRL emissions from the HMSFR sample with (1) source name, (2)(3) the pointing center coordinates, (4) epoch of observations, (5) measured peak antenna temperature of a Gaussian fitting, (6) integral flux of the Gaussian fitting with error, (7) (FWHM) of the Gaussian fitting with error, (8) radio defined LSR velocity at the peak value with error, (9)(10) Bayesian distance and error calculated following Reid et al. (2016) with a default equal weighting ($P_{far} = 0.5$) on near and far distance probability, (11) complementary information: “SL” for side-lobe detected sources, “?” for weak sources without accurate Gaussian line fitting, (12) association with 6.7 GHz methanol maser, (13) other name(s) of the sources, for sources associated with an Anderson2014 source, we label the type of the Anderson2014 counterpart: “K” for “Known” sources, “C” for “candidate” sources, “G” for “Grouped” sources and “Q” for “Radio quiet” sources. For multi-component sources, the components are sorted by peak line intensity.

NOTE—(This table is available in its entirety in a machine-readable form in the online journal and the source files on arXiv.org. A portion is shown here for guidance regarding its form and content.)

Table 4. List of HMSFR sources traced by RRL and/or methanol maser.

414 RRL-only sources											
$l(^{\circ}), b(^{\circ})$	$l(^{\circ}), b(^{\circ})$	$l(^{\circ}), b(^{\circ})$	$l(^{\circ}), b(^{\circ})$	$l(^{\circ}), b(^{\circ})$	$l(^{\circ}), b(^{\circ})$	$l(^{\circ}), b(^{\circ})$	$l(^{\circ}), b(^{\circ})$	$l(^{\circ}), b(^{\circ})$	$l(^{\circ}), b(^{\circ})$	$l(^{\circ}), b(^{\circ})$	$l(^{\circ}), b(^{\circ})$
G18.059+2.035	G18.559+2.029	G18.915+2.027	G20.495+0.157	G20.749-0.112	G21.919-0.324	G22.396+0.334	G22.397+0.300	G22.551-0.522			
G22.835-0.438	G22.873-0.258	G22.877-0.432	G22.953-0.358	G23.009-0.379	G23.039-0.641	G23.096-0.413	G23.172-0.183	G23.240-0.114			
G23.241-0.481	G23.271-0.139	G23.315-0.184	G23.323-0.294	G23.338-0.213	G23.351-0.139	G23.386-0.130	G23.402+0.450	G23.416-0.108			
G23.428-0.231	G23.431-0.519	G23.458+0.066	G23.458-0.016	G23.465+0.115	G23.473-0.212	G23.490-0.028	G23.538-0.004	G23.563+0.008			
G23.601-0.015	G23.696+0.167	G23.740+0.157	G23.771+0.149	G23.823+0.135	G23.868-0.117	G23.873+0.086	G23.899-0.268	G23.900+0.520			
G23.929+0.499	G23.959+0.405	G23.964+0.168	G23.995-0.097	G24.010+0.503	G24.113-0.176	G24.132+0.123	G24.191-0.036	G24.235-0.223			
G24.273-0.137	G24.283-0.009	G24.323+0.047	G24.349+0.020	G24.351-0.269	G24.359+0.127	G24.393+0.013	G24.425+0.243	G24.426+0.351			
G24.427+0.122	G24.443-0.228	G24.470+0.464	G24.479-0.250	G24.499+0.390	G24.519-0.111	G24.520-0.565	G24.546-0.245	G24.554+0.503			
G24.564-0.308	G24.615+0.421	G24.626-0.101	G24.639-0.030	G24.730+0.153	G24.775+0.118	G24.811+0.056	G24.818-0.108	G24.820+0.158			
G24.826-0.073	G24.848-0.102	G24.865+0.145	G24.910+0.037	G25.141-0.400	G25.156-0.273	G25.229+0.175	G25.356+0.263	G25.383-0.377			
G25.392-0.131	G25.664-0.120	G26.087-0.055	G26.327+0.307	G26.331+0.134	G26.353+0.010	G26.374+0.246	G26.526+0.381	G26.579-0.120			
G26.580+0.080	G26.854-0.077	G26.902-0.306	G26.983-0.228	G27.028+0.283	G27.069+0.072	G27.180-0.004	G27.185-0.082	G27.977+0.078			
G28.063-0.085	G28.150+0.169	G28.188-0.212	G28.231+0.039	G28.264-0.182	G28.280-0.154	G28.291+0.010	G28.328-0.075	G28.342+0.101			
G28.393+0.085	G28.413+0.145	G28.439+0.035	G28.452+0.002	G28.577-0.333	G28.579+0.144	G28.585+3.712	G28.688-0.278	G28.692+0.028			
G28.747+0.270	G28.757+0.059	G28.852+3.701	G28.855-0.219	G28.920-0.228	G28.928+0.019	G29.119+0.029	G29.414+0.185	G29.609+0.197			
G29.725+0.074	G29.780-0.260	G29.833-0.261	G29.873+0.032	G29.887-0.005	G29.887-0.779	G29.939-0.870	G29.941-0.071	G30.030-0.383			
G30.103-0.079	G30.136-0.228	G30.145-0.067	G30.197+0.309	G30.301-0.203	G30.338-0.251	G30.339-0.174	G30.365+0.288	G30.392+0.121			
G30.446-0.359	G30.464+0.033	G30.587-0.125	G30.604+0.176	G30.610+0.235	G30.624-0.107	G30.652-0.204	G30.667-0.332	G30.668+0.063			
G30.672+0.014	G30.693+0.228	G30.735-0.295	G30.741-0.195	G30.769+0.105	G30.810+0.046	G30.810+0.314	G30.846-0.075	G30.857+0.004			
G30.902-0.035	G30.912+0.020	G30.920+0.088	G30.927+0.351	G30.945+0.158	G31.036+0.236	G31.041-0.232	G31.101+0.265	G31.122+0.063			
G31.375+0.483	G31.496+0.177	G31.508-0.164	G31.544-0.043	G31.554-0.101	G31.611+0.151	G31.677+0.245	G32.010-0.323	G33.031+0.084			
G33.086+0.001	G33.265+0.066	G33.430-0.016	G33.548+0.021	G34.033-0.024	G34.185+0.114	G34.286+0.129	G34.366-0.058	G34.515+0.066			
G34.530-1.087	G34.546+0.535	G34.712-0.595	G34.719-0.678	G35.067-1.569	G35.291+0.808	G35.360-1.781	G35.442-0.018	G35.467+0.138			
G35.500-0.021	G35.579-0.031	G35.603-0.203	G35.615-0.951	G35.681-0.176	G35.823-0.202	G36.454-0.187	G37.359-0.074	G37.593-0.124			
G37.659+0.119	G37.669-0.093	G37.769-0.263	G37.800-0.372	G39.312-0.216	G39.537-0.378	G39.882-0.346	G40.445+2.528	G40.495+2.570			
" G40.545+2.596	G40.592+ 2.509	G41.355+0.406	G43.177-0.008	G43.181-0.056	G43.262-0.045	G44.241+0.152	G45.124+0.136	G45.525+0.012			
" G45.541-0.016	G48.628+0.214	G48.632-0.587	G48.652-0.315	G48.655-0.728	G48.742-0.512	G48.888-0.410	G48.923-0.445	G48.946-0.331			
G48.961-0.396	G49.025-0.526	G49.028-0.217	G49.072-0.327	G49.224-0.334	G49.268-0.337	G49.341-0.337	G49.368-0.303	G49.391-0.235			
G49.406-0.372	G49.461-0.551	G49.958+0.126	G50.042+0.260	G50.094-0.677	G50.817+0.242	G51.341+0.065	G51.371-0.045	G51.383-0.007			
G52.234+0.759	G52.260-0.521	G52.355-0.588	G52.399-0.936	G52.540-0.927	G52.921-0.621	G53.575+0.069	G54.110-0.081	G59.474-0.185			
G59.582-0.147	G63.153+0.442	G75.840+0.367	G75.841+0.425	G76.659+1.922	G77.973+2.236	G78.161+1.871	G78.231+0.905	G78.259-0.017			
G78.377+1.020	G78.405+0.609	G78.633+0.979	G78.641+0.672	G78.662+0.266	G78.670+0.184	G78.697+1.234	G78.728+0.946	G78.840+0.695			
G78.873+0.754	G78.881+1.427	G78.901+0.661	G79.024+2.449	G79.027+0.436	G79.075+3.462	G79.128+2.278	G79.170+0.396	G79.207+2.146			
G79.246+0.451	G79.312-0.654	G79.330-0.800	G79.362-0.131	G79.385-1.564	G79.393+1.782	G79.545-1.057	G79.561-0.766	G79.699+1.019			
G79.843+0.890	G79.854-1.495	G79.877+2.476	G79.886+2.552	G79.887-1.481	G79.900+1.111	G79.998-1.454	G80.820+0.405	G80.859-0.083			
G80.865+0.342	G80.865+0.420	G80.939-0.127	G81.111-0.145	G81.250+1.123	G81.252+0.982	G81.264-0.136	G81.266+0.931	G81.337+0.824			
G81.341+0.759	G81.435+0.704	G81.469+0.023	G81.512+0.030	G81.525+0.218	G81.548+0.095	G81.582+0.103	G81.601+0.291	G81.663+0.465			

Table 4 continued

Table 4 (continued)

$l(^{\circ}), b(^{\circ})$	$l(^{\circ}), b(^{\circ})$	$l(^{\circ}), b(^{\circ})$	$l(^{\circ}), b(^{\circ})$	$l(^{\circ}), b(^{\circ})$	$l(^{\circ}), b(^{\circ})$	$l(^{\circ}), b(^{\circ})$	$l(^{\circ}), b(^{\circ})$	$l(^{\circ}), b(^{\circ})$	$l(^{\circ}), b(^{\circ})$	$l(^{\circ}), b(^{\circ})$	$l(^{\circ}), b(^{\circ})$	$l(^{\circ}), b(^{\circ})$
G81.683+0.541	G81.685-0.040	G81.722+0.021	G81.840+0.917	G81.876+0.734	G81.898+0.809	G81.918-0.010	G82.069-0.309	G82.186+0.100				
G82.278+2.209	G82.434+1.785	G84.586-1.111	G84.638-1.140	G84.649-1.089	G84.707-0.270	G84.708-1.285	G84.716-0.848	G84.722-1.248				
G84.724-1.138	G84.753+0.253	G84.773-1.046	G84.826-1.137	G84.835-1.187	G84.841-1.085	G84.852+3.697	G84.854-0.744	G84.856-0.500				
G84.870-1.073	G84.929-1.095	G84.941-1.126	G84.941-1.162	G85.019-1.131	G85.021-0.157	G85.081-0.215	G85.082-1.159	G85.112-1.207				
G85.171-1.169	G85.481-1.176	G92.670+3.072	G94.442-5.478	G107.222-0.893	G108.763-0.948	G110.081+0.081	G111.526+0.803	G111.567+0.752				
G113.603-0.616	G118.038+5.108	G123.035-6.355	G123.050-6.310	G126.645-0.786	G133.690+1.113	G133.716+1.207	G133.718+1.137	G133.750+1.198				
G133.948+1.065	G134.004+1.144	G134.219+0.721	G134.239+0.639	G134.279+0.856	G134.469+0.431	G136.918+1.067	G137.585+1.351	G138.297+1.556				
G138.327+1.570	G149.383-0.361	G150.525-0.930	G169.174-0.921	G173.615+2.732	G182.339+0.249	G206.573-16.362	G208.675-19.191	G208.724-19.192				
G208.726-19.232	G208.760-19.216	G208.792-19.243	G208.824-19.256	G208.894-19.313	G209.184-19.494	G213.752-12.616	G213.885-11.832					
103 sources associated with both RRL and methanol maser												
G20.762-0.064	G22.355+0.066	G23.010-0.410	G23.185-0.380	G23.271-0.256	G23.389+0.185	G23.436-0.184	G23.653-0.143	G23.680-0.189				
G23.899+0.065	G23.965-0.110	G24.313-0.154	G24.328+0.144	G24.362-0.146	G24.485+0.180	G24.528+0.337	G24.633+0.153	G24.790+0.084				
G24.943+0.074	G25.177+0.211	G25.346-0.189	G25.395+0.033	G25.709+0.044	G26.545+0.423	G28.147-0.004	G28.287-0.348	G28.320-0.012				
G28.609+0.017	G28.804-0.023	G28.832-0.250	G28.862+0.066	G29.320-0.162	G29.835-0.012	G29.927+0.054	G30.004-0.265	G30.250-0.232				
G30.403-0.297	G30.419-0.232	G30.536-0.004	G30.589-0.043	G30.662-0.139	G30.789+0.232	G30.807+0.080	G30.810-0.050	G30.823+0.134				
G30.866+0.114	G30.897+0.163	G30.959+0.086	G30.973+0.562	G30.980+0.216	G31.076+0.458	G31.159+0.058	G31.221+0.020	G31.237+0.067				
G31.413+0.308	G31.579+0.076	G32.118+0.090	G32.798+0.190	G32.992+0.034	G33.092-0.073	G33.143-0.088	G33.393+0.010	G33.638-0.035				
G34.411+0.235	G35.141-0.750	G35.194-1.725	G35.398+0.025	G35.578+0.048	G37.479-0.105	G37.602+0.428	G38.076-0.266	G38.119-0.229				
G38.202-0.068	G38.255-0.200	G38.258-0.074	G41.121-0.107	G42.692-0.129	G43.076-0.078	G43.089-0.011	G43.148+0.013	G43.178-0.519				
G43.890-0.790	G45.454+0.060	G48.905-0.261	G48.991-0.299	G49.466-0.408	G50.779+0.152	G52.199+0.723	G53.618+0.036	G59.498-0.236				
G75.770+0.344	G78.882+0.723	G78.969+0.541	G79.736+0.991	G80.862+0.383	G81.752+0.591	G81.871+0.779	G84.951-0.691	G84.984-0.529				
G97.527+3.184	G111.532+0.759	G173.596+2.823	G213.706-12.602									
137 methanol-maser-only sources												
G16.872-2.154	G16.883-2.186	G17.021-2.402	G173.482+2.446	G173.617+2.883	G174.205-0.069	G183.349-0.575	G20.234+0.085	G20.363-0.014				
G20.926-0.050	G21.023-0.063	G21.370-0.226	G213.752-12.615	G22.050+0.211	G24.148-0.009	G24.634-0.323	G25.256-0.446	G25.410+0.105				
G25.498+0.069	G25.613+0.226	G25.649+1.050	G25.837-0.378	G26.421+1.686	G26.598-0.024	G26.623-0.259	G26.645+0.021	G27.220+0.261				
G27.222+0.136	G27.287+0.154	G27.725+0.037	G27.784+0.057	G27.795-0.277	G28.180-0.093	G28.393+0.085	G28.843+0.494	G29.281-0.330				
G29.941-0.070	G30.370+0.483	G30.770-0.804	G30.788+0.203(R)	G30.819+0.273	G30.972-0.141	G31.253+0.003(L)	G31.253+0.003(R)	G32.045+0.059				
G32.773-0.059	G32.828-0.315	G33.229-0.018	G33.322-0.364	G33.425-0.315	G33.641-0.228	G33.726-0.119	G34.096+0.018	G34.229+0.133				
G34.757+0.025	G34.789-1.392	G34.974+0.365	G35.149+0.809	G35.197-0.729	G35.225-0.360	G35.247-0.237	G35.792-0.174	G36.137+0.564				
G36.634-0.203	G36.705+0.096	G36.833-0.031	G36.919+0.483	G37.043-0.035	G37.430+1.517	G37.554+0.201	G37.763-0.215	G38.598-0.213				
G38.933-0.361	G39.100+0.491	G39.387-0.141	G40.282-0.220	G40.425+0.700	G40.597-0.719	G40.622-0.138	G40.964-0.025	G41.307-0.169				
G42.035+0.191	G43.037-0.453	G43.808-0.080	G45.070+0.124	G45.360-0.598	G45.493+0.126	G45.804-0.356	G49.043-1.079	G49.265+0.311				
G49.537-0.904	G49.599-0.249	G50.034+0.581	G51.678+0.719	G52.663-1.092	G52.922+0.414	G53.022+0.100	G53.141+0.071	G53.485+0.521				
G54.371-0.613	G56.963-0.234	G58.775+0.647	G59.436+0.820	G59.634-0.192	G59.785+0.068	G59.833+0.672	G62.310+0.114	G69.543-0.973				
G71.522-0.385	G73.063+1.796	G74.098+0.110	G75.010+0.274	G76.093+0.158	G78.122+3.633	G81.794+0.911	G82.308+0.729	G84.193+1.439				
G85.394-0.023	G89.930+1.669	G90.921+1.487	G94.609-1.790	G98.036+1.446	G99.070+1.200	G108.184+5.518	G108.758-0.986	G109.839+2.134				
G109.868+2.119	G110.196+2.476	G111.256-0.770	G121.329+0.639	G123.035-6.355	G123.050-6.310	G124.015-0.027	G134.029+1.072	G136.859+1.165				
G137.068+3.002	G149.076+0.397											

NOTE—For sources showing multiple methanol emissions, “R” and “L” label the right/left hand side of the components (see Yang et al. 2017, 2019)

Table 5. Characteristics of Helium and Carbon RRL emissions.

Name	R.A.	Decl.	Epoch	T_b	S_i	ΔV	ν_p	d	σ_d	Type	Maser	Other Name(s)
(1,b)	(J2000)	(J2000)	(dd/mm/yy)	(mK)	(K km s ⁻¹)	(km s ⁻¹)	(km s ⁻¹)	(kpc)	(kpc)	(11)	(12)	(13)
(° , °)	(h m s)	(° ' ")										
(1)	(2)	(3)	(4)	(5)	(6)	(7)	(8)	(9)	(10)	(11)	(12)	(13)
G20.749-0.112	18:29:21.28	-10:52:38.5	04/07/16	20	0.70(0.06)	33.4(3.5)	-68.4(1.3)	3.46	0.20	He		(K) G020.728-00.105 / Kes 68
G23.428-0.231	18:34:48.38	-08:33:22.0	21/08/16	15	0.24(0.06)	15.2(3.8)	-20.0(1.9)	5.93	0.23	He		(K) G023.423-00.216
G23.436-0.184	18:34:39.21	-08:31:40.4	21/08/16	14	0.17(0.04)	10.8(2.1)	-24.6(1.3)	5.87	0.24	He	yes	(K) G023.458-00.179
G23.473-0.212	18:34:49.22	-08:30:28.2	21/08/16	9	0.17(0.04)	17.6(4.6)	-19.8(2.0)	5.86	0.24	He		(K) G023.458-00.179
G23.563+0.008	18:34:12.06	-08:19:36.6	06/08/16	13	0.30(0.04)	21.6(3.6)	-34.1(1.3)	5.60	0.40	He		(K) G023.572-00.020
G24.479-0.250	18:36:49.63	-07:37:55.3	31/08/16	15	0.16(0.03)	10.0(1.7)	-26.7(1.1)	5.83	0.24	He		(K) G024.493-00.219
G24.790+0.084	18:36:12.46	-07:12:10.8	05/09/16	28	0.50(0.06)	16.4(2.1)	-15.1(0.9)	6.04	0.23	He	yes	(K) G024.844+00.093
G25.346-0.189	18:38:12.83	-06:50:00.8	05/09/16	17	0.40(0.05)	22.4(3.5)	-64.9(1.7)	3.83	0.29	He	yes	(K) G025.382-00.151 / IRAS 18354-0652
G25.392-0.131	18:38:05.54	-06:45:58.3	06/09/16	22	0.61(0.11)	26.5(6.8)	-22.1(2.1)	8.88	0.31	He		(K) G025.382-00.151
				23	0.20(0.06)	7.9(3.3)	-55.7(1.0)			C		

NOTE—Properties of the He and C RRL components with (1) source name, (2)(3) the pointing center coordinates, (4) epoch of observations, (5) measured peak antenna temperature of a Gaussian fitting, (6) integral flux of the Gaussian fitting with error, (7) (FWHM) of the Gaussian fitting with error, (8) radio defined LSR velocity at the peak value with error, (9)(10) Bayesian distance and error calculated using peak velocity of corresponding H RRLs. The distances were derived following Reid et al. (2016) with a default equal weighting ($P_{far} = 0.5$) on near and far distance probability, (11) emission type: “He” and “C” label the He and C RRLs respectively, (12) association with 6.7 GHz methanol maser, (13) other name(s) of the sources, for sources associated with an Anderson2014 source, we label the type of the Anderson2014 counterpart: “K” for “Known” sources, “C” for “candidate” sources, “G” for “Grouped” sources and “Q” for “Radio quiet” sources.

NOTE—(This table is available in its entirety in a machine-readable form in the online journal and the source files on arXiv.org. A portion is shown here for guidance regarding its form and content.)

Table 6. Characteristics of the PNe candidates

Name	R.A.	Decl.	Epoch	T_b	S_i	ΔV	ν_p	d	σ_d	Notes	Other Name(s)
(1)	(2)	(3)	(4)	(5)	(6)	(7)	(8)	(9)	(10)	(11)	(12)
(l,b)	(J2000)	(J2000)	(dd/mm/yy)	(mK)	(mK km s ⁻¹)	(km s ⁻¹)	(km s ⁻¹)	(kpc)	(kpc)		
([◦] , [′])	(h m s)	([◦] ′ ″)									
G30.035−0.002	18:46:09.37	−02:34:44.4	17/09/16	47	1.32(0.07)	26.3(1.6)	97.1(0.6)	6.82	1.31	PNe?	PN G030.0+00.0 / (K) G030.022 / IRAS 18436-0239
G78.911+0.792	20:29:08.19	+40:15:26.5	16/09/16	18	0.40(0.04)	20.8(2.9)	10.7(1.3)	2.72	0.97	PNe?	PN Sd 1 / (K) G078.886+00.709
G78.931+0.722	20:29:29.59	+40:13:55.0	16/09/16	32	1.05(0.07)	30.7(2.2)	17.2(1.0)	3.07	0.87	PNe?	PN Sd 1 / (K) G078.886+00.709
G84.913−3.505	21:07:00.13	+42:13:01.8	14/12/17	35	2.24(0.05)	58.7(1.5)	25.5(0.7)	1.28	0.07	PNe	NGC 7027
G84.946−3.488	21:07:03.27	+42:15:12.1	15/12/17	38	2.23(0.09)	55.6(2.4)	22.4(1.0)	1.28	0.07	PNe	NGC 7027

NOTE—Characteristics of the potential PNe sample with (1) source name, (2)(3) the pointing center coordinates, (4) epoch of observations, (5) measured peak antenna temperature of a Gaussian fitting, (6) integral flux of the Gaussian fitting with error, (7) (FWHM) of the Gaussian fitting with error, (8) radio defined LSR velocity at the peak value with error, (9)(10) Bayesian distance and error calculated following Reid et al. (2016) with a default equal weighting ($P_{far} = 0.5$) on near and far distance probability, (11) source type: “PNe” for sources associated explicitly with a PNe, “PNe?” for potential PNe sources, (12) other name(s) of the sources, for sources associated with an Anderson2014 source, we label the type of the Anderson2014 counterpart: “K” for “Known” sources, “C” for “candidate” sources, “G” for “Grouped” sources and “Q” for “Radio quiet” sources.

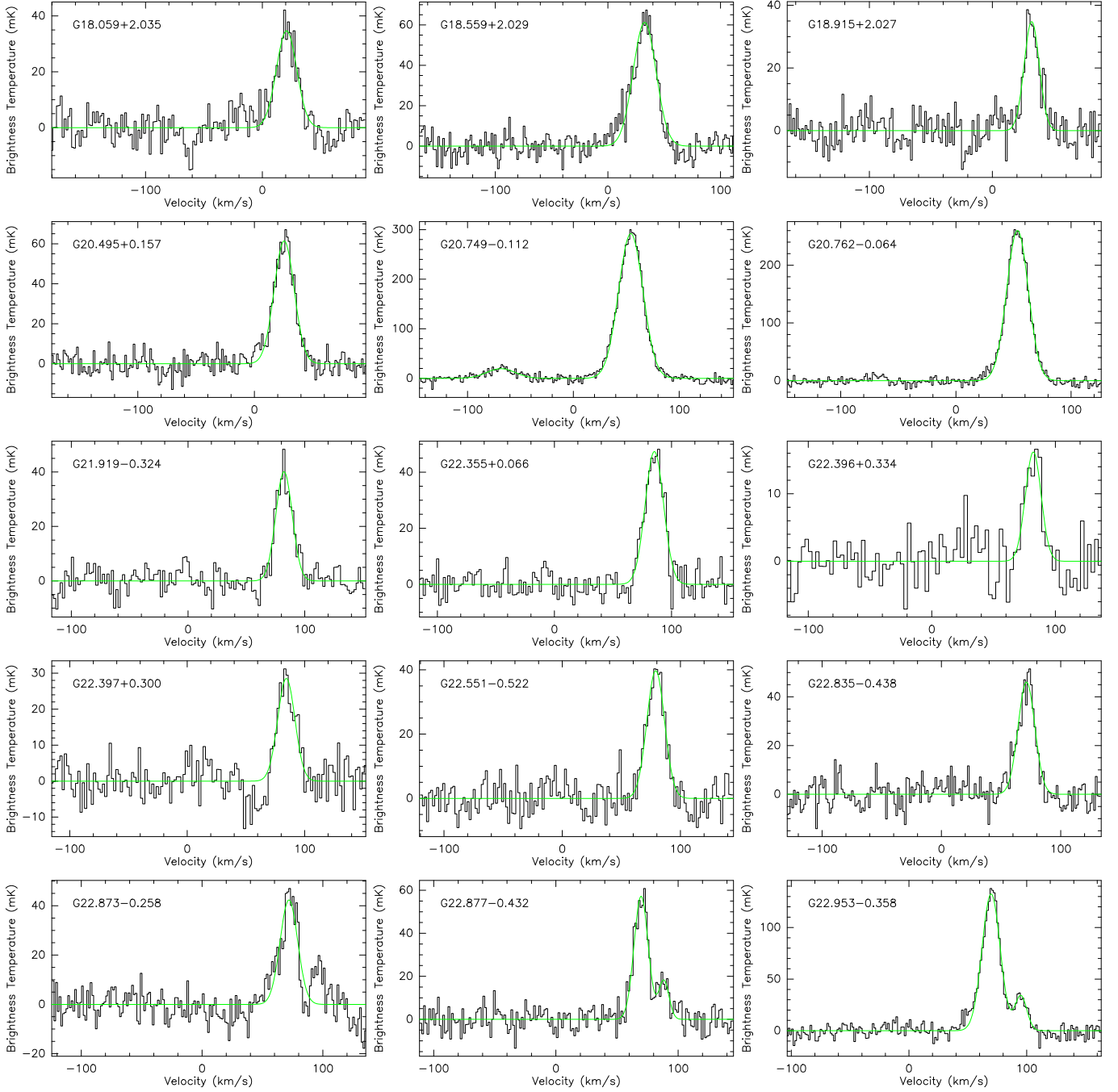
Table 7. Characteristics of the SNR candidates

Name	R.A.	Decl.	Epoch	T_b	S_i	ΔV	ν_p	d	σ_d	Notes	Other Name(s)
($^{\circ}$, $^{\circ}$)	(J2000) (h m s)	(J2000) ($^{\circ}$ ' ")	(dd/mm/yy)	(mK)	(mK km s $^{-1}$)	(km s $^{-1}$)	(km s $^{-1}$)	(kpc)	(kpc)		
(1)	(2)	(3)	(4)	(5)	(6)	(7)	(8)	(9)	(10)	(11)	(12)
G30.726+0.103	18:47:02.74	-01:54:56.2	18/08/16	75	1.86(0.01)	23.5(0.4)	117.8(0.4)	7.19	0.82	SNR?	SNR G030.3+00.7 / (K) G030.796+00.183 / IRAS 18445-0158
G79.831+1.280	20:29:53.77	+41:17:18.8	08/09/16	40	1.10(0.06)	25.6(1.7)	-16.9(0.7)	5.28	0.63	SNR?	SNR G079.8+01.2 / (K) G080.362+01.212
G28.532+0.129	18:42:56.49	-03:51:21.7	19/09/16	26	0.83(0.06)	30.1(2.1)	101.0(1.0)	8.13	0.31	SNR?	MAGPIS G28.5167+0.1333 / (K) G028.581+00.145
G28.565+0.021	18:43:23.21	-03:52:32.3	19/09/16	86	2.59(0.06)	28.3(0.8)	96.9(0.3)	8.09	0.37	SNR?	SNR G028.56+00.00 / (K) G028.607+00.019
G27.102+0.024	18:40:41.50	-05:10:32.5	09/09/16	42	1.41(0.07)	31.1(1.8)	92.9(0.7)	8.55	0.39	SNR?	MAGPIS G27.1333+0.0333

NOTE—Characteristics of the potential SNR sample with (1) Source name, (2)(3) the pointing center coordinates, (4) epoch of observations, (5) measured peak antenna temperature of a Gaussian fitting, (6) integral flux of the Gaussian fitting with error, (7) (FHM) of the Gaussian fitting with error, (8) radio defined LSR velocity at the peak value with error, (9)(10) Bayesian distance and error calculated following Reid et al. (2016) with a default equal weighting ($P_{far} = 0.5$) on near and far distance probability, (11) source type, all the sources in this table are candidate sources thus are marked with “SNR?”, (12) other name(s) of the sources, for sources associated with an Anderson2014 source, we label the type of the Anderson2014 counterpart: “K” for “Known” sources, “C” for “candidate” sources, “G” for “Grouped” sources and “Q” for “Radio quiet” sources. For multi-component sources, the components are sorted by peak line intensity.

APPENDIX

Appendix A: RRL spectra for the HMSFR sample.



NOTE—This figure is available in its entirety in the online journal. A portion is shown here for guidance regarding its form and content.

Figure 17. RRL spectra for the HMSFRs.

Appendix B: RRL spectra for the previously known and potential PNe sources.

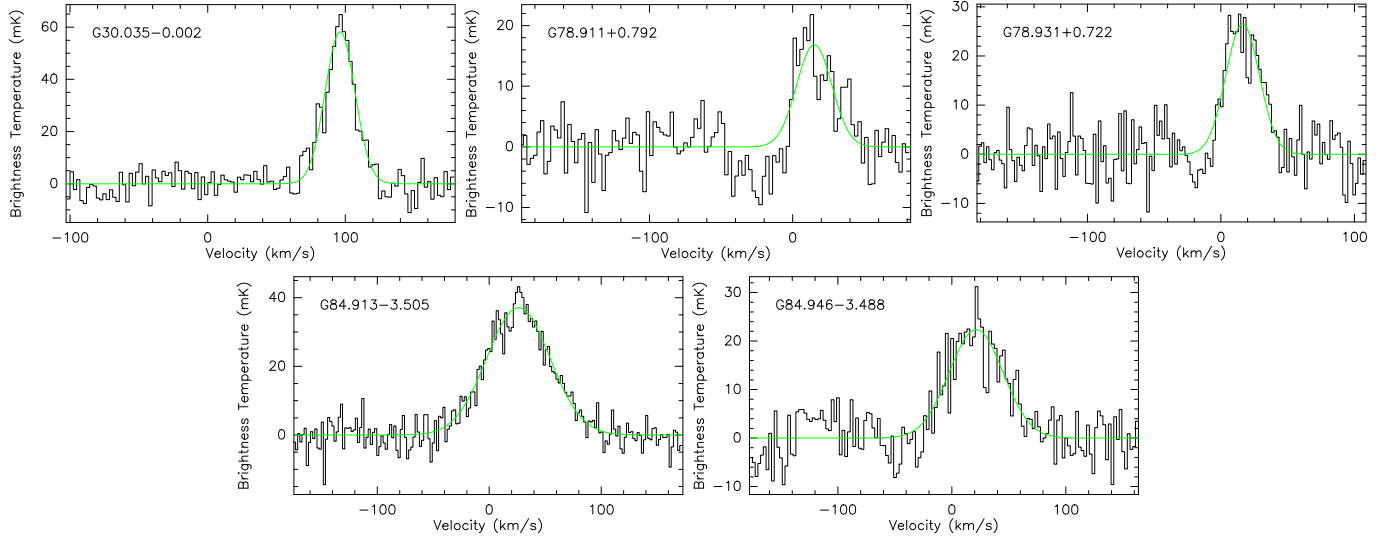


Figure 18. RRL spectra for the candidate PNe sources.

Appendix C: RRL spectra for the potential SNR sources.

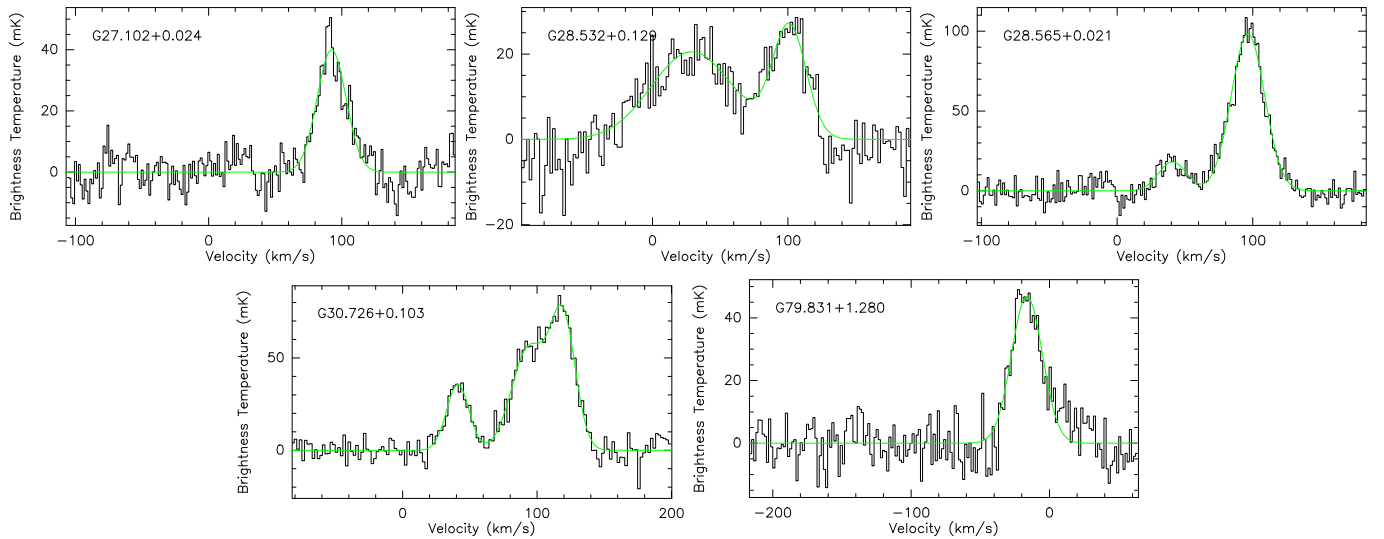


Figure 19. RRL spectra for the candidate SNR sources.